



Profiling of formaldehyde, glyoxal, methylglyoxal, and CO over the Amazon: Normalised excess mixing ratios and related emission factors in biomass burning plumes

Flora Kluge¹, Tilman Hüneke^{1,i}, Matthias Knecht^{1,ii}, Michael Lichtenstern², Meike Rotermund¹, Hans Schlager², Benjamin Schreiner¹, and Klaus Pfeilsticker¹

¹Institute of Environmental Physics, University of Heidelberg, Heidelberg, Germany

²Institut für Physik der Atmosphäre, Deutsches Zentrum für Luft- und Raumfahrt (DLR), Oberpfaffenhofen, Germany

ⁱnow with Encavis AG, Hamburg, Germany

ⁱⁱnow with Ernst & Young, GmbH, Wirtschaftsprüfungsgesellschaft, Stuttgart, Germany

Correspondence: Flora Kluge
(fkluge@iup.uni-heidelberg.de)

Abstract. We report on airborne measurements of tropospheric mixing ratios and vertical profiles of CH_2O , $\text{C}_2\text{H}_2\text{O}_2$, $\text{C}_3\text{H}_4\text{O}_2^*$, and CO over the Amazon Basin during the ACRIDICON-CHUVA campaign from the German High Altitude and Long-range research aircraft (HALO) in fall 2014. The joint observation of in situ CO and remotely measured CH_2O , $\text{C}_2\text{H}_2\text{O}_2$, and $\text{C}_3\text{H}_4\text{O}_2^*$, together with visible imagery and air mass back trajectory modelling using NOAA HYSPLIT (National Oceanic
5 Atmospheric Administration, HYbrid Single-Particle Lagrangian Integrated Trajectory) allow us to discriminate between the probing of background tropical air, in which the concentration of the measured species results from the oxidation of biogenically emitted VOCs (mostly isoprene), and measurements of moderately to strongly polluted air masses affected by biomass burning emissions or the city plume of Manaus. For twelve near surface measurements of fresh biomass burning plumes, normalised excess mixing ratios of $\text{C}_2\text{H}_2\text{O}_2$ and $\text{C}_3\text{H}_4\text{O}_2^*$ with respect to CH_2O are inferred and compared to recent studies. The
10 mean $R_{\text{GF}}=0.07$ (range 0.02–0.11) is in good agreement with recent reports which suggest R_{GF} to be significantly lower than previously assumed in global CTM models. The mean $R_{\text{MF}}=0.98$ (range 0.09–1.50) varies significantly during the different observational settings, but overall appears to be much larger (up to a factor of 5) than previous reports suggest even when applying a correction factor of 2.0 ± 0.5 to account for the additional dicarbonyls included in the $\text{C}_3\text{H}_4\text{O}_2^*$ measurements. Using recently reported emission factors of CH_2O for tropical forests, our observations suggest emission factors of $\text{EF}_{\text{G}}=0.25$
15 (range 0.11 to 0.52) g kg^{-1} for $\text{C}_2\text{H}_2\text{O}_2$, and $\text{EF}_{\text{M}} = 4.7$ (range 0.5 to 8.64) g kg^{-1} for $\text{C}_3\text{H}_4\text{O}_2^*$. While EF_{G} agrees well with recent reports, EF_{M} is (like R_{MF}) slightly larger than reported in other studies, presumably due to the different plume ages or fuels studied. Our observations of these critical carbonyls and intermediate oxidation products may support future photochemical modelling of air pollution over tropical vegetation, as well as validate past and present space-borne observations of the respective species.



20 1 Introduction

Emissions from biomass burning are a large source of reactive gases and particulate matter to the atmosphere on a local, regional and up to the global scale (Crutzen and Andreae, 1990; Andreae and Merlet, 2001; Andreae et al., 2001; Andreae, 2019). Pyrogenic emissions form a complex mixture of species that can change over the duration of the fire and undergo further chemical reactions as emissions are transported downwind. In consequence, biomass burning may have adverse effects on the atmospheric photochemistry, secondary aerosol formation and composition, and hence cloud formation and radiation, as well as human health. Therefore, accurate measurements of pyrogenic emissions, the evolution of fire plume composition and the formation and aging of aerosols are needed, but respective data are lacking for many species (e.g., Andreae and Merlet (2001); Akagi et al. (2011); Stockwell et al. (2015); Andreae (2019)).

Among the manifold of species emitted in large amounts by fires are carbonyl compounds such as formaldehyde (CH_2O), glyoxal ($\text{C}_2\text{H}_2\text{O}_2$), methylglyoxal ($\text{C}_3\text{H}_4\text{O}_2$), 2,3-butanedione ($\text{C}_3\text{H}_6\text{O}_2$), and many others (e.g., Andreae (2019)). Here and further on, $\text{C}_3\text{H}_4\text{O}_2^*$ denotes $\text{C}_3\text{H}_4\text{O}_2$ and other substituted dicarbonyls (cf. 2,3-butanedione) with visible absorption spectra similar to $\text{C}_3\text{H}_4\text{O}_2$, since they cannot be distinguished with the spectral resolution available in our limb measurements (sect. 2.1).

It is well known that in the atmosphere most of CH_2O is formed as an intermediate oxidation species from the degradation of CH_4 and from a suite of non-methane hydrocarbons (NMHCs) (Seinfeld and Pandis, 2013). CH_2O can further be directly emitted into the troposphere by biomass burning (e.g., Finlayson-Pitts and Pitts (2000); Andreae and Merlet (2001); Wagner et al. (2002); Akagi et al. (2011); Seinfeld and Pandis (2013); Stockwell et al. (2015)), and from incomplete combustion as well as the direct emission by vegetation (Carlier et al. (1986) and references therein). Due to its short lifetime in the atmosphere of only several hours, CH_2O mixing ratios range from several 10 ppt to a few 100 ppt in the pristine (e.g., marine) environment. In the lower or polluted troposphere, mixing ratios might reach several ppb (e.g., Finlayson-Pitts and Pitts (2000); Jaeglé et al. (1997); Wagner et al. (2002); Borbon et al. (2012); Seinfeld and Pandis (2013) and others). Secondary formed CH_2O (for example from acetone photolysis) is an important source of HO_x radicals, in particular in the middle and upper troposphere (Jaeglé et al., 1997). Further, since CH_2O is considerably water soluble, it may participate in either acid or base catalysed aldol-condensation reactions in the aerosol phase, hence contributing to secondary organic aerosol (SOA) formation (Wang et al., 2010). Numerous studies of formaldehyde emissions from biomass burning both in the laboratory and the field were undertaken in the past, and its emission factor appears to be fairly well established for the various studied fuel and fire types (e.g., Finlayson-Pitts and Pitts (2000); Andreae and Merlet (2001); Wagner et al. (2002); Akagi et al. (2011); Seinfeld and Pandis (2013); Stockwell et al. (2015); Andreae (2019)). Based on this knowledge, models have generally been able to reproduce reasonably well the formaldehyde column densities observed by satellites (e.g., Dufour et al. (2009); Stavrou et al. (2009); Boeke et al. (2011); Bauwens et al. (2016), and others), or concentrations directly measured in the atmosphere (e.g., Arlander et al. (1995); Fried et al. (2008); Borbon et al. (2012); Kaiser et al. (2015); Chan Miller et al. (2017) and others).

Similar to formaldehyde, glyoxal and methylglyoxal are formed by 47 % and 79 %, respectively, during the oxidation of isoprene emitted by vegetation (Fu et al. (2008); Wennberg et al. (2018)). Recent air-borne and satellite measurements



identified the Amazon to be the world most prominent isoprene source region, with mixing ratios exceeding 6 ppb isoprene in
55 the boundary layer by end of the dry season in September 2014 (Gu et al., 2017; Fu et al., 2019). These elevated mixing ratios
are a consequence of the large isoprene emission from the rain forest combined with a significantly prolonged atmospheric
lifetime of up to 36 hours (GEOS-Chem model simulations) over the Amazon Basin compared to the global mean of less than
4 hours (Fu et al. (2019), fig. 6a). Fu et al. (2019) suspected strong isoprene emissions combined with low NO_x concentrations
to lead to significantly suppressed OH-levels as possible reason for the observed slower isoprene oxidation in this regime. The
60 longer isoprene lifetime and efficient vertical transport over the Amazon lead to elevated isoprene mixing ratios not only within
the boundary layer but also in higher altitudes (Fu et al. (2019), fig. 4d), where it is a possible source for in situ glyoxal and
methylglyoxal production in the free troposphere.

The second most important precursors of the trace gases are acetylene (mostly anthropogenically emitted) for glyoxal and
acetone (mostly biogenic) for methylglyoxal, but both gases are also formed during the oxidation of other volatile organic
65 compounds (VOCs), particularly alkenes, aromatics, and monoterpenes (Fu et al., 2008). For both gases, Fu et al. (2008)
estimated their global source strengths to 45 Tg a^{-1} and 140 Tg a^{-1} , respectively. Atmospheric lifetimes of glyoxal and
methylglyoxal are only about 2 h, mostly due to photolysis and to a lesser degree due to reactions with OH radicals (Koch and
Moortgat, 1998; Volkamer et al., 2005a; Tadić et al., 2006; Fu et al., 2008; Wennberg et al., 2018). Accordingly, in ambient air
 $\text{C}_2\text{H}_2\text{O}_2$ and $\text{C}_3\text{H}_4\text{O}_2$ mixing ratios typically do not exceed several 100 ppt (Fu et al., 2008).

70 Glyoxal and methylglyoxal are additionally emitted in considerable quantities by biomass burning, their individual emission
strengths however are not yet well established (e.g., Andreae and Merlet (2001); Akagi et al. (2011); Stockwell et al. (2015);
Zarzana et al. (2017, 2018); Andreae (2019)). The recent compilation of emission factors by Andreae (2019) indicates for most
reported fuels the complete lack of emission data for both dicarbonyls. Until the recent laboratory and field studies by Zarzana
et al. (2017, 2018), previous information on the glyoxal and methylglyoxal emissions from biomass burning were based on
75 only two laboratory studies (McDonald et al., 2000a; Hays et al., 2002). While (Hays et al., 2002) reported larger emission
factors for glyoxal compared to methylglyoxal, the recent findings of Zarzana et al. (2017, 2018) indicated significantly smaller
glyoxal emissions but larger emissions of methylglyoxal and other substituted dicarbonyls in fires of agricultural biomass than
those previously assumed in models (Fu et al., 2008).

Satellite and aircraft measurements of formaldehyde and glyoxal complemented by modelling have been used to study their
80 different atmospheric sources (e.g., Stavrakou et al. (2009); Boeke et al. (2011); Lerot et al. (2010); Chan Miller et al. (2014);
Bauwens et al. (2016); Stavrakou et al. (2016), and others), the secondary aerosol formation from carbonyls (typically in the
background atmosphere), as well as in biomass burning plumes (Knote et al., 2014; Li et al., 2016; Lim et al., 2019), and
even more recently to estimate the organic aerosol abundance (Liao et al., 2019). Unlike for formaldehyde, the models had
varying success in reproducing the glyoxal column densities (Myriokefalitakis et al., 2008; Stavrakou et al., 2009; Lerot et al.,
85 2010). In comparison to satellite measurements from SCIAMACHY and GOME-2, several studies have found that the models
underestimate global glyoxal emissions, when not considering additional secondary sources apart from those inferred from the
oxidation of biogenic precursors.



The ratios of $C_2H_2O_2$ to CH_2O (R_{GF}), and $C_3H_4O_2$ to CH_2O (R_{MF}) can be used as indications of the precursor VOC species and to identify biomass burning in contrast to biogenic sources (Kaiser et al., 2015). In the past, R_{GF} has been studied based on multiple ground-based observations as well as satellite measurements (e.g., McDonald et al. (2000a); Kaiser et al. (2015); Chan Miller et al. (2017)). Kaiser et al. (2015) studied inferred R_{GF} over the south-eastern United States during the 2013 SENEX (Southeast Nexus) campaign, and compared these measurements to respective OMI (Ozone Monitoring Instrument) satellite retrievals. They concluded, that in regimes rich of monoterpene emissions R_{GF} is generally larger than 3 %, while regions dominated by isoprene oxidation appear characterized by low $R_{GF} < 3$ %. For a compilation of previously inferred R_{GF} see Kaiser et al. (2015), Table 1.

More recently, Stavrakou et al. (2016) examined emissions of crop residue fires in the North China Plain using data from the OMI satellite, which is part of the so called A-train (<https://atrain.nasa.gov/>). Their inferred column emission ratio of 0.04–0.05 was comparable to the R_{GF} observed by Zarzana et al. (2017), but smaller than those reported by McDonald et al. (2000a) and Hays et al. (2002), which were used in the study of Fu et al. (2008). Nevertheless, the chemical transport model used by Stavrakou et al. (2016) was able to reproduce the measured formaldehyde column densities and the glyoxal enhancements observed over the North China Plain during the peak burning season.

Information on methylglyoxal in the atmosphere is even more rare, since to our knowledge satellite instruments measuring methylglyoxal are not (yet) available, and atmospheric measurements of methylglyoxal are still sparse. This is a result of the moderate spectral resolution of space- and air-borne optical measurements, which suffer from the spectral interference of the major but only weakly structured absorption bands of methylglyoxal with those of other dicarbonyls (mainly 2,3-butanedione) in the blue spectral region (Meller et al., 1991; Horowitz et al., 2001; Thalman et al., 2015; Zarzana et al., 2017). Potential interferences with the 7ν absorption band of water vapour at 442 nm further complicate the spectral retrieval (Thalman et al., 2015; Zarzana et al., 2017). In situ measurements of methylglyoxal using different techniques have only recently become available (Thalman and Volkamer, 2010; Pang et al., 2011; Lawson et al., 2015; Michoud et al., 2018). The very limited number of measurements in conjunction with insufficient detection limits are still preventing comprehensive studies of methylglyoxal.

Here we report on simultaneous measurements of CO, CH_2O , $C_2H_2O_2$, and $C_3H_4O_2^*$ in the lower to upper troposphere over the Amazon Basin at the end of the dry season in 2014. All measurements were performed from the german research aircraft HALO operated by the Deutsches Zentrum für Luft- und Raumfahrt (DLR). The simultaneous near surface measurements of $C_2H_2O_2$ and $C_3H_4O_2^*$ allow us to estimate their emission ratios with respect to CH_2O as well as the normalized excess mixing ratios within the probed biomass burning plumes, and when combined with previously reported emission factors (e.g., Andreae (2019)), to estimate their emission factors for tropical forest fires. The joint measurements of the carbonyls and CO in the middle and in the upper troposphere, more distant from their direct sources at the ground, provides insight into their tropospheric profiles and precursors in a pristine atmosphere and under low NO_x conditions. Additionally, air mass backward trajectory modelling classifies the probed air masses and their possible origins.

The paper is organized as follows. Chapter 2 briefly describes the measurement techniques and methods used in the present study. Chapter 3 and 4 report on the ACRIDICON-CHUVA campaign and the actual measurements, and chapter 5 discusses the major findings and results. Chapter 6 concludes and summarises the study.



Table 1. Trace gas absorption cross sections used for the DOAS based spectral retrieval.

No.	Absorber	Temperatur [K]	Reference	Uncertainty [%]
1	O ₄	273	Thalman and Volkamer (2013)	4
2	O ₃	203	Serdyuchenko et al. (2014)	3
3	O ₃	273	Serdyuchenko et al. (2014)	3
4	NO ₂	273	Burrows et al. (1998)	4
5	H ₂ O	293	Rothman et al. (2009)	
6	CH ₂ O	293	Chance and Orphal (2011)	10
7	C ₂ H ₂ O ₂	296	Volkamer et al. (2005b)	3
8	C ₃ H ₄ O ₂	296	Meller et al. (1991)	10
9	C ₄ H ₆ O ₂	223	Horowitz et al. (2001)	4

2 Methods

2.1 DOAS Measurements

125 The mini-DOAS instrument is a UV/vis/near-IR six channel optical spectrometer, which detects scattered skylight received from scanning limb and nadir directions. These spectra can be analysed for absorption structures of O₄, CH₂O, C₂H₂O₂ and C₃H₄O₂* (among other species). A video camera (type uEye UI-1005XS from IDS Imaging Development Systems GmbH) with a field of view of 46° is installed into the telescope unit and co-aligned with the spectrometer's limb telescopes. It provides visual imagery of the probed atmospheric scene at a rate of 1 Hz. An extensive description of the instrument and its deployment
130 on the HALO aircraft can be found in Hüneke (2016); Hüneke et al. (2017). The mini-DOAS instrument remotely probes the atmosphere with the limb telescopes (FOV 0.5° vertical, 3.15° horizontal) oriented perpendicular and right hand to the aircraft main axis. Although the limb telescopes can be directed at any elevation angle for traditional atmospheric profiling, during the ACRIDICON-CHUVA campaign they were constantly directed at 0.3° below the horizon, for optimal measurements when using the O₄ scaling method (Hüneke (2016); Hüneke et al. (2017); Stutz et al. (2017); Werner et al. (2017), and below).

135 The post-flight analysis of the collected limb spectra includes a DOAS (Differential Optical Absorption Spectroscopy (Platt and Stutz, 2008)) analysis of the measured skylight spectra for the absorption structures of O₄, CH₂O, C₂H₂O₂, and C₃H₄O₂* as well as the attribution of the measured absorption to the correct locations in the atmosphere. The latter is performed using the O₄ scaling method described in detail in Hüneke (2016); Hüneke et al. (2017); Stutz et al. (2017) as well as below. The DOAS analysis of the data is performed according to the settings in Tables 1 and 2.

140 Exemplary sample retrievals of CH₂O, C₂H₂O₂, and C₃H₄O₂* are shown in fig. 1. The detection of C₃H₄O₂* (fig. 1, panel (3)) deserves a brief discussion. It is known that substituted dicarbonyls such as biacetyl (CH₃COCOCH₃), with absorption cross sections in the visible spectral range similar to those of C₃H₄O₂, are also co-emitted from biomass fires in significant quantities (e.g., Meller et al. (1991); Horowitz et al. (2001); Thalman et al. (2015); Zarzana et al. (2017)). Owing to the mod-



Table 2. Details of the DOAS spectral analysis for the various trace gases.

Target gas	Spectral interval [nm]	Fitted absorbers (see Table 1)	Add. Param.	Polyn.	σ [dSCD]
O ₄	348–369	1, 2, 3, 4, 6	I _{O_{fs}} ⁽ⁱ⁾ , R ⁽ⁱⁱ⁾ , R · λ ⁴⁽ⁱⁱⁱ⁾	2	8 × 10 ⁴¹
	460–490	1, 2, 3, 4, 5	I _{O_{fs}} , R, R · λ ⁴	2	4 × 10 ⁴¹
CH ₂ O	324–354	1, 2, 3, 4, 6	I _{O_{fs}} , R, R · λ ⁴	2	5 × 10 ¹⁵
C ₂ H ₂ O ₂	420–439 and 447–465	1, 3, 4, 5, 7	I _{O_{fs}} , R, R · λ ⁴	2	1 × 10 ¹⁵
C ₃ H ₄ O ₂ [*]	420–475	1, 3, 4, 5, 7, 8, 9	I _{O_{fs}} , R, R · λ ⁴	2	1 × 10 ¹⁶

(i) I_{O_{fs}}: Offset spectrum; (ii) R: Ring spectrum; (iii) R · λ⁴: Ring spectrum multiplied by λ⁴.

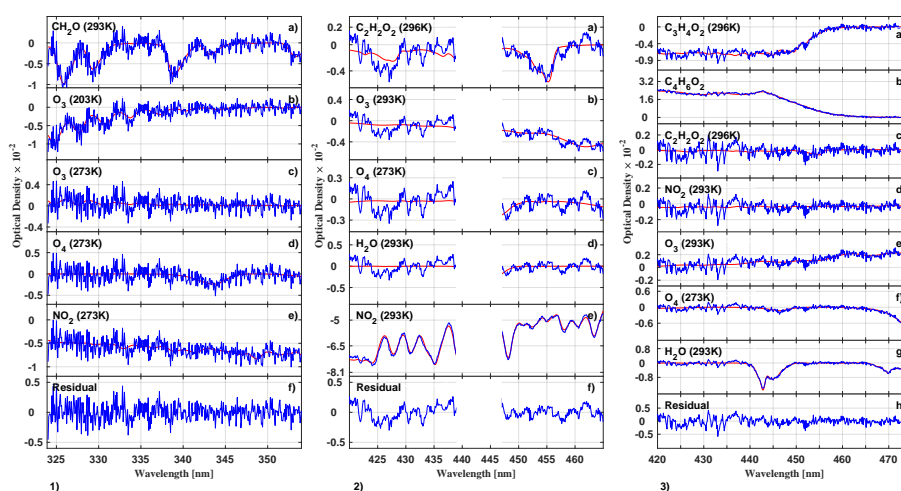


Figure 1. Inferred absorption spectra of CH₂O (1), C₂H₂O₂ (2), and C₃H₄O₂^{*} (3) for the measurements at 17:16, 15:06 and 14:53 UTC, respectively, during the flight on Sept. 11, 2014 (AC11). The traces shown in blue are the inferred atmospheric spectra together with the residual spectral structures, the red line shows the reference spectra of the respective gases. In order to avoid cross correlations with the 7ν absorption band of H₂O at 442 nm, C₂H₂O₂ is simultaneously fit over two separated spectral windows, ranging from 420 nm to 439 nm and 447 nm to 465 nm.

erate resolution of our spectrometer in the visible spectral range (full width half maximum resolution of 1.1 nm or 8.4 pixels, see Hüneke (2016)), we cannot separately (and thus unambiguously) detect these substituted dicarbonyls in the atmosphere, unlike in studies employing higher resolving spectrometers (e.g., Thalman et al. (2015)). Accordingly, we report here the weighted sum (absorption cross section times concentration) of C₃H₄O₂ and that of other substituted dicarbonyls and express that quantity as C₃H₄O₂^{*}.

From the retrieved slant column densities, absolute concentrations of the targeted gases are inferred using the recently developed O₄ scaling method. As shown in previous studies, the scaling method is based on simultaneous measurements of the target gas X and a scaling gas P of known concentration (here the collision complex O₂–O₂, briefly called O₄) in the same



wavelength interval (Hüneke, 2016; Hüneke et al., 2017; Stutz et al., 2017; Werner et al., 2017). The concentration $[X_j]$ of the trace gas X in the atmospheric layer j is then determined from

$$[X]_j = \frac{\alpha_{X_j}}{\alpha_{P_j}} \cdot \frac{SCD_X}{SCD_P} \cdot [P]_j \quad (1)$$

155 (see Stutz et al. (2017), eq. (14)). Here, $[P]_j$ is the calculated extinction of O_4 ($\epsilon_{O_4} = \sigma \cdot k_{eq} \cdot [O_2]_j^2$) in the atmospheric layer j, from which we take the sample. SCD_P is the measured optical depth of O_4 and SCD_X is the measured slant column density of the target gas X. The α -factors α_{X_j} and α_{P_j} each express the ratio of the absorption of the gas in layer j to the total atmospheric absorption. Usually, the α -factors are simulated in supporting radiative transfer calculations using the Monte Carlo model McArtim (Deutschmann et al., 2011; Knecht, 2015).

160 When applying the scaling method to air-borne UV/vis spectroscopy in limb geometry, a powerful radiative transfer model is necessary to treat the radiative transfer in 2D or 3D, calculate the refraction and also account for the sphericity of the Earth. We use the Monte Carlo radiative model McArtim (Deutschmann et al., 2011), where each measurement is modelled forward while considering the actual atmospheric, instrumental, and observational (e.g., Sun position relative to the pointing) parameters, the geolocation and the pointing of the telescope as described in Hüneke (2016); Hüneke et al. (2017). Further, a
165 combination of climatological aerosol profiles obtained by LIVAS (Amiridis et al., 2015) and the Stratospheric Aerosol and Gas Experiment II (SAGE II) (https://eosweb.larc.nasa.gov/project/sage3/sage3_table) is considered. For the calculation of the α -factors, box air mass factors are simulated and summed, weighted by concentration (Stutz et al. (2017), eq. (11)). We calculate the extinction $[P]_j$ to obtain the vertical O_4 profile. For the target gases CH_2O , $C_2H_2O_2$, $C_3H_4O_2^*$, we assume exponentially
170 photochemical lifetimes, the time scales of possible vertical transport, as well as when inspecting the profile shapes obtained in the post-analysis (fig. 9).

Evidently, UV/vis limb measurements naturally divide the atmosphere into three different layers, which are separated by the different contributions to the total absorption or optical depth (OD). These contributions are (a) the overhead absorption (OD_{oh}), (b) the absorption located within the line-of-sight of the telescopes (OD_{limb}) (of which most, but not all is due to
175 single scattering), and (c) the absorption below the line of sight (OD_{ms}) (of which the photon paths are necessarily all of higher scattering order). For a high-flying aircraft, OD_{oh} has the least uncertainty since O_4 absorption approximately scales with $[O_2]^2$ and the optical state of the overhead atmosphere is well known. Therefore, the remainder of the measured total O_4 absorption has to be due to the varying contributions of (b) and (c), which are mostly modulated by the current low level cloud cover and ground albedo (Stutz et al. (2017), fig. 7). The knowledge of the α -factor however gives a handle on the relative fractions (b) and
180 (c), since contribution (b) can be calculated from $OD_{limb} = \alpha \cdot OD_{meas}$, and accordingly $OD_{ms} = OD_{meas} - OD_{oh} - OD_{limb}$. Still, the calculated attributions of (b) and (c) to OD_{meas} can only be approximated due to the assumptions made regarding the current aerosols distribution and the cloud coverage. Figure 2 illustrates the contributions to OD_{meas} at 343.7 nm (panel (1a)) and 477.3 nm (panel (2a)) as a function of the flight time for Sept. 16, 2014. Figure 3 shows the same data, but sorted by flight altitude to demonstrate the relative change of the contributions. For both investigated wavelengths, the absorption within the
185 line of sight of the telescopes to the total O_4 absorption dominates with $> 50\%$ up to 10 km altitude, with a relative minimum

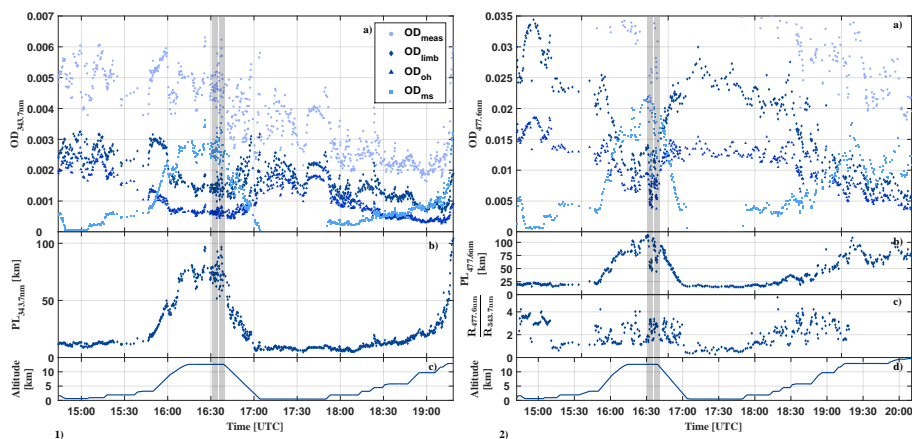


Figure 2. Attribution of the total measured optical depth of O_4 at 343.7 nm (panel (1) on the left) and at 477.6 nm (panel (2) on the right) to the various fractions, i.e., absorption from overhead the aircraft (OD_{oh}), from multiple scattering below the aircraft (OD_{ms}), within the line-of-sight of the telescopes (OD_{limb}), and the total measured optical depth of O_4 (OD_{meas}) for the HALO flight on Sept. 16, 2014 (AC11) (panels (1a), (2a)). Average line-of-sight photon path length inferred from the measured OD_{meas} at 343.7 nm and 477.6 nm, respectively, as a function of the flight time (panels (1b), (2b)). The colour ratio $\frac{R_{343.7}}{R_{477.6}}$ of the measured radiances at 343.7 nm versus 477.6 nm is shown in panel (2c). The flight trajectory of the HALO aircraft is shown in panels (1c) and (2d). The sharp drop of the optical depth between 16:32–16:34 UTC and 16:35–16:39 UTC (grey bars) coincides with the passage of a cumulonimbus cloud in front of the telescopes. For details see the text.

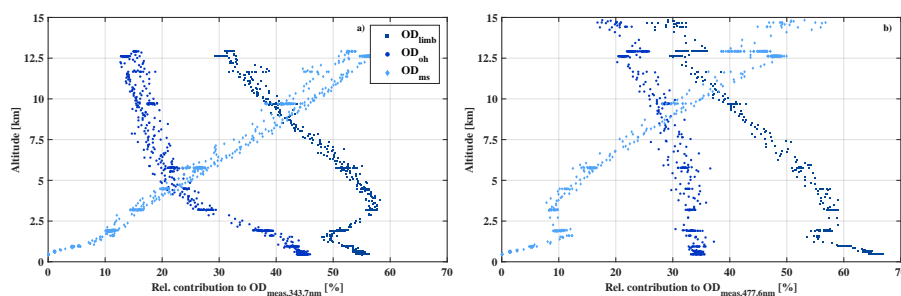


Figure 3. Relative contribution to the limb measured optical depth of O_4 at 343.7 nm (panel (a)) and at 477.6 nm (panel (b)) due to the absorption overhead the aircraft (OD_{oh}), from multiple scattering (OD_{ms}), and within the line of sight of the telescopes (OD_{limb}) for the HALO flight on Sept. 11, 2014 (AC11). For details see the text.

seen at the top of the planetary boundary layer at approximately 2 km, where often stratocumulus clouds prevail over the Amazon. Further, a maximum of OD_{limb} is visible at about 4 km, most probably a result of the increasing horizontal visibility with altitude and the moderate contribution of reflected multiple scattered photons from the lower atmosphere to the total O_4 absorption. In the upper troposphere, the relative contribution of OD_{limb} to OD_{meas} decreases while the effective horizontal



atmospheric aerosol content, the cloud structure and coverage and their optical properties, it is more reasonable to speak here of an indication rather than a determination of the photon path lengths.

Fortunately, these uncertainties do not propagate into the uncertainty of the α -factor ratio and hence into the determination of $[X]_j$, provided the gases X and P have similar profile shapes (Knecht, 2015; Hüneke et al., 2017; Stutz et al., 2017). From the
195 above discussion, it also becomes clear that our air-borne UV/vis limb measurements average over some atmospheric volume, which precludes direct comparisons with in situ measured quantities on spatial scales smaller than the current averaging volume. This is of relevance to our study, for example when adding information from in situ measurements like CO to the analysis of our data.

Summing-up all described uncertainties, the precision error of the combined methods is calculated according to eq. (1) as

$$200 \quad [\Delta X]_j = \sqrt{\left(\frac{\Delta\alpha_{R,j}}{\alpha_{R,j}}\right)^2 + \left(\frac{\Delta S_{X,j}}{S_{X,j}}\right)^2 + \left(\frac{\Delta S_{P,j}}{S_{P,j}}\right)^2 + \left(\frac{\Delta P_j}{P_j}\right)^2} \cdot [X]_j, \quad (2)$$

where $\Delta\alpha_{R,j}$ accounts for (a) random Mie extinction, (b) small scale variability of the target and scaling gas mixing ratios at flight level and (c) uncertainty in the sampling contribution as discussed in fig. 2 and 3. The slant column errors $\Delta S_{X,j}$ and $\Delta S_{P,j}$ account for (a) uncertainty of the inferred fraunhofer reference SCD and (b) the DOAS Fit error. ΔP_j accounts for the uncertainty of the in situ mixing ratio of the scaling gas, which in the case of O_4 scales with the air density and is
205 accordingly limited by the measurement uncertainty of pressure and temperature. Additionally, the systematic errors of the individual absorption cross sections need to be added to $\Delta S_{X,j}$ according to Table 1. An extensive discussion of the total error budget of the O_4 scaling can be found in Hüneke (2016). While ΔP_j and $\Delta\alpha_{R,j}$ contribute approximately constantly to the total error budget, $\Delta S_{X,j}$ strongly increases with decreasing slant column density. For mixing ratios below 1 ppb (CH_2O), 0.15 ppb ($C_2H_2O_2$), and 1.3ppb ($C_2H_4O_2^*$), the total precision error is strongly dominated by $\Delta S_{X,j}$. For higher mixing ratios, $\Delta\alpha_{R,j}$
210 and $\Delta S_{X,j}$ contribute in equal parts in the cases of $C_2H_2O_2$ and $C_2H_4O_2^*$. For CH_2O , $\Delta\alpha_{R,j}$ is the major error factor for mixing ratios above 1 ppb, and $\Delta S_{X,j}$ only makes up 30 % of the total error. For all gases, ΔP_j never exceeds 7 % of the total precision error. Due to the strong dependence of $\Delta S_{X,j}$ on the slant column density and the exponentially decreasing vertical profiles of the gases, the resulting total precision errors $[\Delta X]_j$ are strongly altitude dependent (fig. 4). They range from 16 % to 100 % for CH_2O , 17 % to 100 % for $C_2H_2O_2$, and 16 % to 100 % for $C_2H_4O_2^*$. This study focuses on measurements below
215 2 km altitude, with mean total errors of the analysed biomass burning events on the order of 21 % for CH_2O (upper and lower limit of the total precision errors are 350 ppt and 740 ppt), 25 % for $C_2H_2O_2$ (total errors from 30 ppt to 45 ppt), and 22 % for $C_2H_4O_2^*$ (total errors from 240 ppt to 560 ppt).

2.2 AMTEX CO Measurements

In situ CO measurements were performed using an Aero-Laser 5002 vacuum UV resonance fluorescence instrument (Gerbig
220 et al., 1996, 1999) installed in the cabin of the HALO aircraft. Main components of the CO instrument include a fluorescence chamber, resonance lamp, optical filter, two dielectric mirrors, and a pump. Atmospheric air is sampled through a backward-facing inlet mounted on top of the HALO fuselage. CO molecules in the ambient air are excited in the chamber by radiation from a radio frequency discharge resonance lamp. The wavelength range (centre line 151 nm with a bandwidth of 9 nm) is

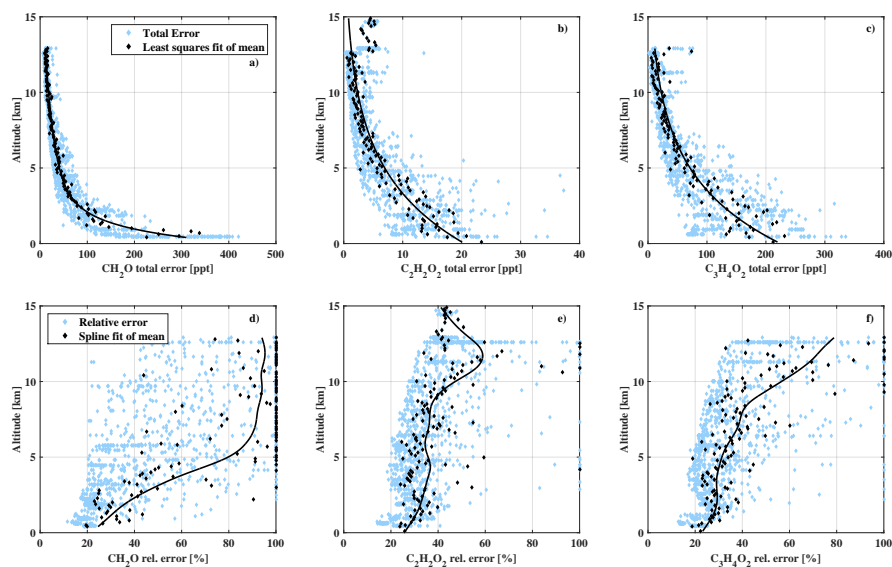


Figure 4. Relative and absolute total precision error of all measurements as a function of the measurement altitude.

selected by the optical filter and the mirrors. The fluorescence signal is detected by a photomultiplier. The flow rate of the
225 sample air through the fluorescence chamber is set to 40 mL min^{-1} (STP). The sample air is dried with a SICAPENT trap
(granulated phosphorus pentoxide drying agent) to eliminate a cross-sensitivity to water vapour.

The CO measurements are made at 1 Hz with a precision of 1.5 ppb. The accuracy is given by the precision and systematic
errors caused by the drift of the background signal and sensitivity of the instrument, and the uncertainty of the CO calibration
standard. The total accuracy amounts to $1.5 \text{ ppb} \pm 2.4\%$ (Gerbig et al., 1999). The CO instrument has been deployed during
230 many aircraft campaigns using the DLR Falcon (e.g. Huntrieser et al. (2016a, b)) and was used for the first time used on board
HALO during the ACRIDICON-CHUVA campaign (Wendisch et al., 2016).

3 Measurements

The ACRIDICON-CHUVA aircraft campaign took place from the operational basis Manaus (Brazil) within the period September
and early October 2014 with a total of 14 scientific flights over the Amazon region. An overview of all ACRIDICON-
235 CHUVA flight tracks can be found in Wendisch et al. (2016), fig. 6. The campaign aimed to improve the understanding of
tropical deep convective clouds and their interaction with biogenic and anthropogenic aerosols, and also included precipita-
tion formation and air pollution studies. A detailed description of the campaign objectives, the participating instruments and
research groups is given in Wendisch et al. (2016).

Our study requires simultaneous measurements of CH_2O , $\text{C}_2\text{H}_2\text{O}_2$, $\text{C}_3\text{H}_4\text{O}_2^*$ and O_4 (performed by the mini-DOAS spec-
240 trometers in the UV and visible spectral ranges as described in sect. 2.1) as well as CO measurements (performed by the



AMTEX instrument, see sect. 2.2), but either of the instruments occasionally failed. Therefore, only for a subset of flights joint data is available. Further, since a part of the flights focused on objectives other than near surface air pollution, here we only present data from four out of the 14 ACRIDICON-CHUVA flights, i.e. those of Sept. 11th (AC09), 16th (AC11), 18th (AC12), and 19th (AC13) in 2014. Nevertheless, the data collected during these flights provides valuable information on the different
245 measured pollutants, their sources, atmospheric transformation and transport in pristine background air in the troposphere as well as fresh and aged air affected by biomass burning in the Amazon.

Each of these measurement flight took seven to eight hours, typically occurring between 14 UTC and 22 UTC, i.e. during daytime. The long flight time supported the sampling of a large geographical area of the rain forest during the four flights, reaching from approximately 6° S to 8° N, and 49° W to 63° W. The detailed flight tracks and respective altitudes are shown
250 in fig. 5. During each of these flights, the probed altitudes ranged from several 100 m up to 15 km, with flight sections inside the planetary boundary layer overpassing large agricultural areas (AC12 and AC13) as well as the rain forest and the Amazon river delta (AC09 and AC11, fig. 5).

Due to the relatively large, but patchy cloud cover over the Amazon, the UV and vis limb radiances varied significantly during the flights. Therefore, typical integration times of the measured co-added sets of skylight spectra range from seconds
255 (under clear sky conditions) to several minutes (during cloudy sky and hazy conditions). In consequence, the along track resolution of the measurements was typically several kilometres in addition to the horizontal resolution perpendicular to the aircraft determined by radiative transfer (sect. 2.1). For the biomass burning events AC11-1 to AC11-3 (Table 3 and sect. 5.4), a two-dimensional visualization of the resulting averaging (or probed) areas per single measurement is indicated by the blue areas in fig. 6. The identification of the atmospheric measurement conditions and in particular of each biomass burning event is
260 based on visual imagery using the recorded video data stream (fig. 7). In the following, only those measurements are claimed to be affected by biomass burning, for which the actual plumes are visible in the recorded images and are in the telescope's line of sight. These events are listed in Table 3. Depending on the flight pattern and the integration time of the spectra, some of these plumes were intercepted more than once. In total, eight distinct plumes were probed during twelve individual measurements, all of which were recorded below 2 km flight altitude.

265 The MODIS instrument on board the Terra and Aqua satellites (MCD14, collection 6, available online from <https://worldview.earthdata.nasa.gov/>, doi:10.5067/FIRMS/MODIS/MCD14DL.NRT.006) reports additional fires in the vicinity of the aircraft trajectory, which were not directly located within in the field of view of the mini-DOAS telescopes, nor within the larger field of view of the camera. Therefore, these events are not more closely investigated in our analysis. However, the emissions of these fires are likely to
270 have created an atmospheric background generally affected by differently aged biomass burning emissions within the boundary layer (fig. 6). Further insights into the recent photochemical past of the air masses are provided by 3 h backward air mass trajectories calculated using the READY (Real-time Environmental Applications and Display sYstem) website of the NOAA HYSPLIT model (<https://www.ready.noaa.gov/HYSPLIT.php>) (Stein et al., 2015; Rolph et al., 2017). Exemplary 3 h backward trajectories are shown for events AC11-1.2 to AC11-3.2 in fig. 6. They indicate, that prior to detection all air masses resided
275 well within the boundary layer, but did not directly pass over any additional reported fire.

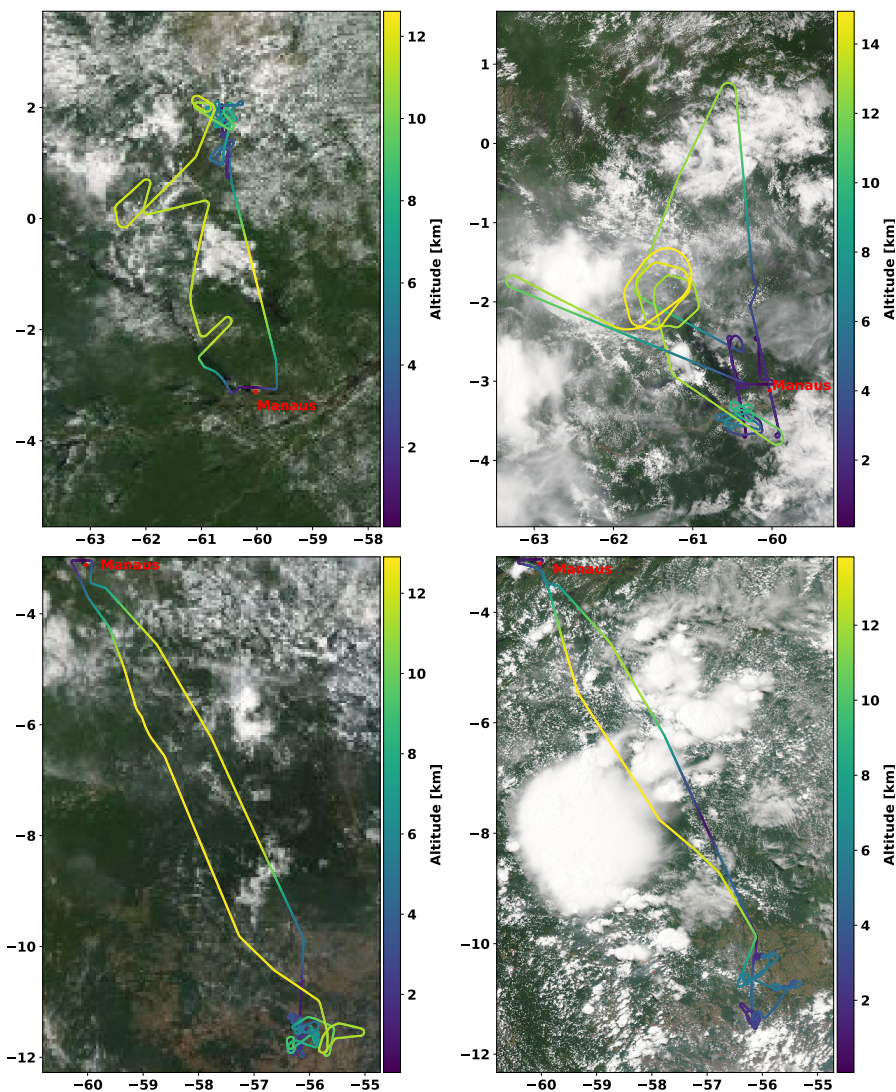


Figure 5. Tracks of the ACRIDICON-CHUVA flights (a) on Sept. 11, 2014, (b) on Sept. 16, 2014 (AC11), (c) on Sept. 18, 2014 (AC12), and (d) on Sept. 19, 2014 (AC13). All flights started and ended at the operational base Manaus airport in Brazil (red dot). The colour coding indicates the flight altitude. The MODIS satellite images are taken from NASA WORLDVIEW and are updated daily, see <https://worldview.earthdata.nasa.gov/>.

However, all identified biomass burning events show large and correlated enhancements of CH_2O , $\text{C}_2\text{H}_2\text{O}_2$, and $\text{C}_3\text{H}_4\text{O}_2^*$, with mixing ratios up to 4.0 ppb, 0.26 ppb, and 2.8 ppb, respectively (fig. 8). Due to the differently sized spatial resolutions of both instruments (sect. 2), the detected peaks in CO and those of CH_2O , $\text{C}_2\text{H}_2\text{O}_2$, and $\text{C}_3\text{H}_4\text{O}_2^*$ do not (and are not expected to) strictly correlate. Therefore, we refrain from directly estimating emission ratios with respect to CO.

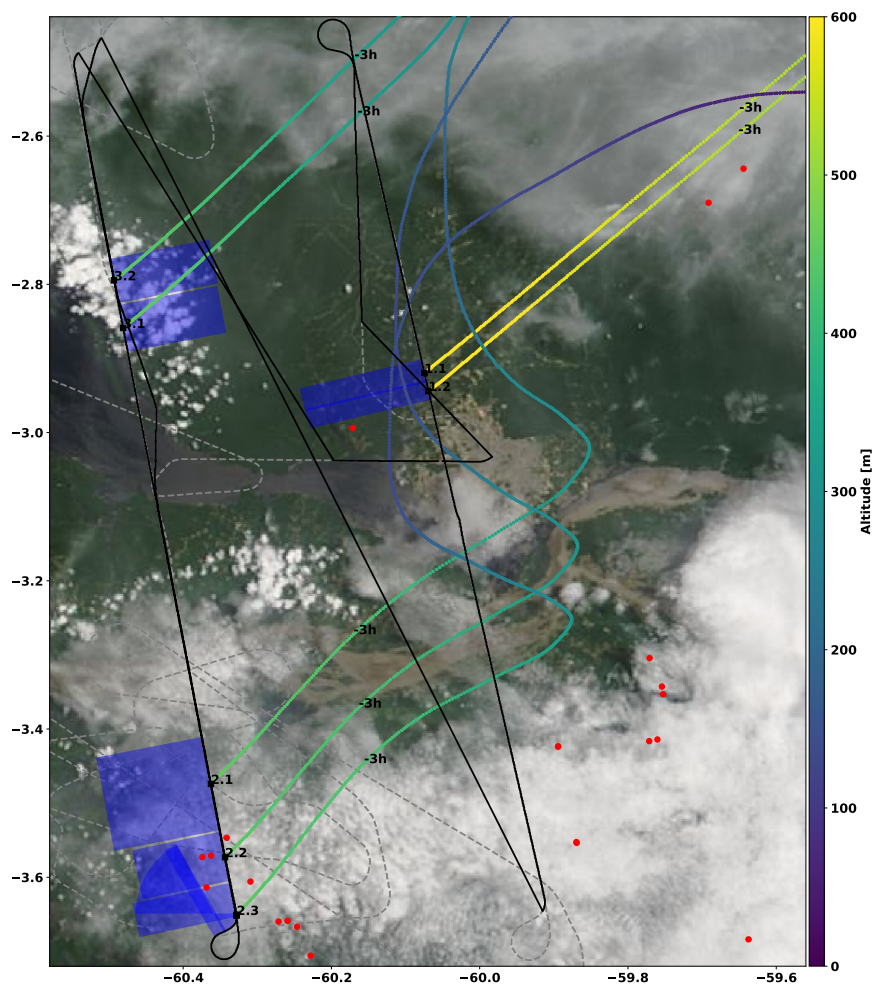


Figure 6. Zoom of the flight track for AC11 on Sept. 16, 2014. The flight tracks below/above 1000 m altitude are labelled by drawn/dashed lines, respectively. The take-off and landing of the aircraft was from Manaus airport (3.1° S, 60.0° W) located in the centre of the image. The biomass burning events detected by the MCD14 MODIS instrument on the Terra and Aqua satellites are indicated with red dots (not to scale). The biomass events probed by the mini-DOAS instrument are marked by black numbers next to the flight track, according to the labelling of Table 3. The blue rectangles approximately indicate the probed air masses in the horizontal plane, where the distance perpendicular to the flight track is given by the O_4 estimated photon path lengths (14 to 19 km), and the along track distance (3 to 15 km) by the spectrum integration time (33 to 166 s) multiplied by the aircraft ground speed (approximately 95 m s^{-1}) (sect. 2.1). For each biomass burning event, 3 h backward air mass trajectories were calculated and plotted colour-coded by the altitude of the air mass. The MODIS satellite image was taken from NASA WORLDVIEW, see <https://worldview.earthdata.nasa.gov/>.



Figure 7. Images taken by the mini-DOAS camera during events 1–6 (as indicated in fig. 6 and 8) for the flight AC11 with the UTC time given in each image. The second image was taken from the respective flight report. The video camera points into the same direction as the three limb telescopes of the mini-DOAS spectrometer, however with a much larger field of view of $\sim 46^\circ$ width.

280 4 Results

Figure 8 shows the inferred volume mixing ratios of CH_2O (panel (a)), $\text{C}_2\text{H}_2\text{O}_2$ (panel (b)), $\text{C}_3\text{H}_4\text{O}_2^*$ (panel (c)), and CO (panel (d)) for flight AC11 on Sept. 16, 2014. The measured trace gas mixing ratios are the largest for flight sections within the planetary boundary layer (14:45 to 15:15 UTC and 17:05 to 17:45 UTC), and the lowest in the upper troposphere (16:15 to 16:45 UTC and 19:15 to 20:20 UTC). Notable are the peaks in CO while flying through the Manaus city plume (grey bars) or biomass burning plumes (red bars). Elevated mixing ratios of CH_2O , $\text{C}_2\text{H}_2\text{O}_2$, and $\text{C}_3\text{H}_4\text{O}_2^*$ can be related to biomass burning as well as to air masses of presumably aged background air (labelled with the green bars) as evidenced by the only moderately elevated CO. Here, the numbers (1) to (6) in panel (a) of fig. 8 denote biomass burning affected air (1–3), air of the Manaus city plume (4), pristine air of the upper troposphere (5), and boundary layer air above the tropical forest (6). Sky images of all six different situations are shown in fig. 7.

290 4.1 Vertical profiles

Below 450 m altitude, CO mixing ratios range from 88.6 ppb to 291.8 ppb (fig. 9, panel (a)), with a mean of $[\text{CO}] = 188.1$ ppb. Within the planetary boundary layer, CO mixing ratios increase from 88.4 ppb to 2308 ppb (mean $[\text{CO}] = 212.8$ ppb), with peak mixing ratios above 500 ppb appearing when biomass burning plumes are passed directly. Lowest $[\text{CO}]$ mixing ratios

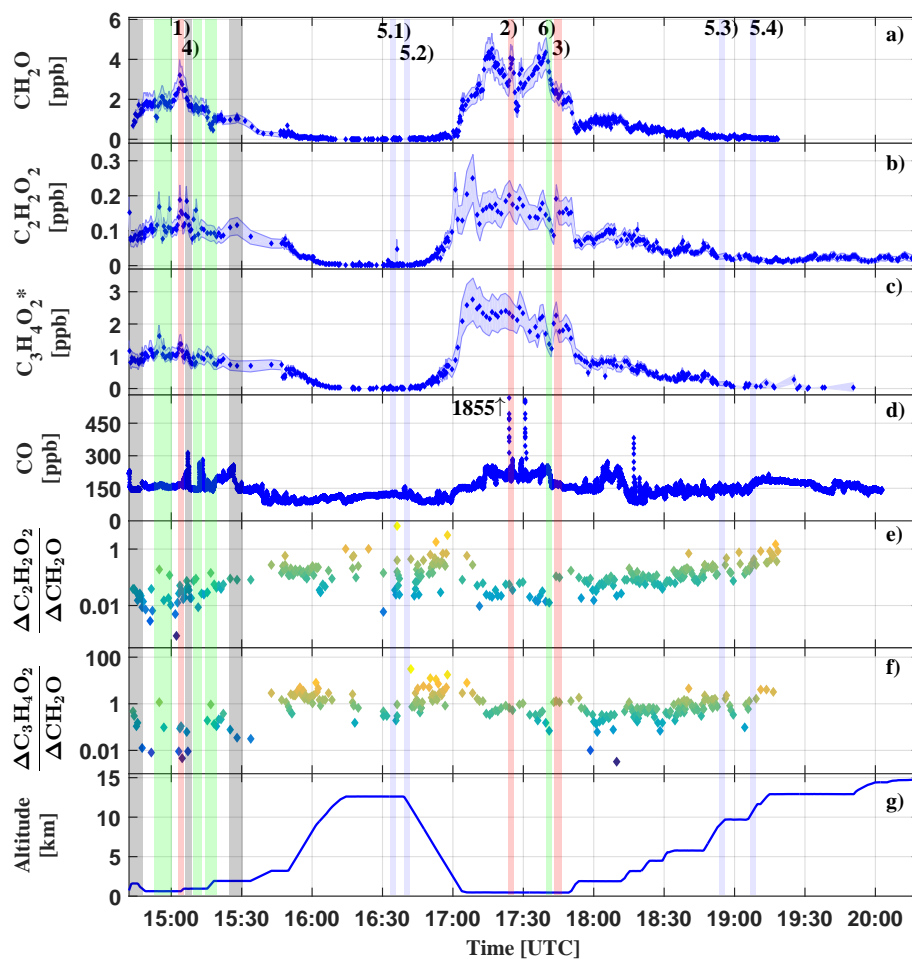


Figure 8. Measured mixing ratios of CH_2O (panel (a)), $\text{C}_2\text{H}_2\text{O}_2$ (panel (b)), $\text{C}_3\text{H}_4\text{O}_2^*$ (panel (c)), CO (panel (d)), inferred $R_{\text{GF}} = \Delta\text{C}_2\text{H}_2\text{O}_2/\Delta\text{CH}_2\text{O}$ (panel (e)), $R_{\text{MF}} = \Delta\text{C}_3\text{H}_4\text{O}_2^*/\Delta\text{CH}_2\text{O}$ (panel (f)), and the height versus time trajectory for the HALO flight AC11 (panel (g)). All measurements within the Manaus city plume are marked by grey bars (e.g. event AC11-4). Examples for measurements in aged air masses of the upper troposphere are marked in blue (e.g. events AC11-5.1–5.4), and green for the general background atmosphere i.e. tropical forest affected air (e.g. event AC11-6). All measurements of biomass burning plumes are labelled in red (events AC11-1, AC11-2 and AC11-3). The event numbers correspond to the labelling in Table 3 and fig. 7. The colour coding in panels (e), and (g) corresponds to the inferred R_{GF} or R_{MF} of each measurement, in order to emphasize the differences in the gas ratios otherwise not clearly distinguishable due to the logarithmic scale of the y-axis.

in the range of 55.1 ppb to 231.9 ppb (mean $[\text{CO}] = 86.3$ ppb) are found in the middle troposphere between 6 and 8 km
 295 altitude. In the upper troposphere (12–14 km), CO increases from 52.5 ppb to 212.6 ppb (mean $[\text{CO}] = 134.5$ ppb). In the
 convective tropics, C-shaped CO profiles are a well-known phenomenon, caused by the rapid transport of near surface CO rich
 air by meso-scale convective systems into the upper troposphere (e.g., Brocchi et al. (2018); Krysztofiak et al. (2018)). When

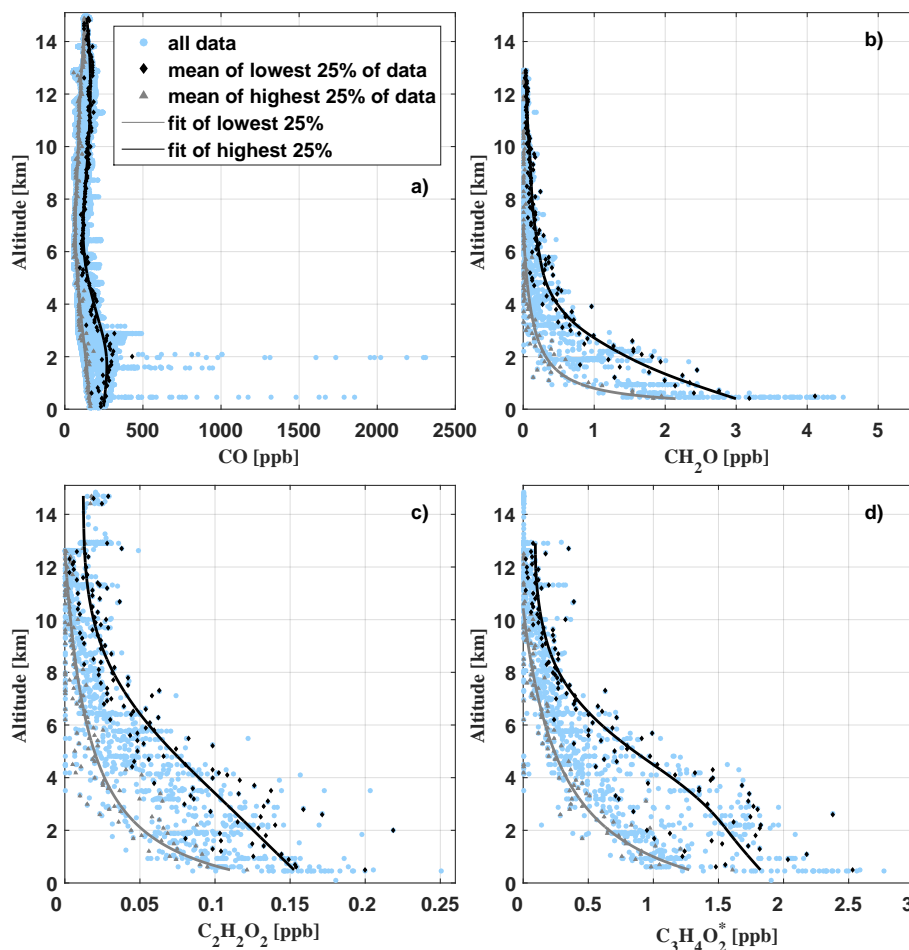


Figure 9. Vertical profiles of CO (panel (a)), CH₂O (panel (b)), C₂H₂O₂ (panel (c)), and C₃H₄O₂^{*} (panel (d)) as measured during flights AC09, AC11, AC12, and AC13 (blue circles). For AC09, there are no CO data available. The grey lines indicate a spline fit (panel (a)) and least squares fits (panel (b) to (d)) through the lower quartile of the data (grey triangles) in 100 m altitude bins. The black line shows corresponding fits through the mean of the upper quartile (black diamonds).

binning the data in 100 m altitude intervals and averaging over the lower and upper data quartiles within each interval, another maximum forms around the top of the boundary layer. Most likely, this suggests that over the Amazon biomass burning plumes often detrain their pollutants near the top of the boundary layer (cf. see for example the image at 17:24 UTC, fig. 7).

Inferred [CH₂O] ranges from 4.5 ppb near the surface to mean mixing ratios of 30 ppt in the upper troposphere (above 10 km). Mixing ratios within the boundary layer and middle troposphere vary significantly (fig. 9, panel (b)). In part, this might be a manifestation of the direct emission of CH₂O into the lower part of the atmosphere, or the in situ formation of CH₂O during the oxidation of biogenic VOCs (BVOCs) as well as partly oxidized VOCs (OVOCs). Figure 10 puts our CH₂O measurements over the Amazon into the context of previously published CH₂O observations all over the world. Within this

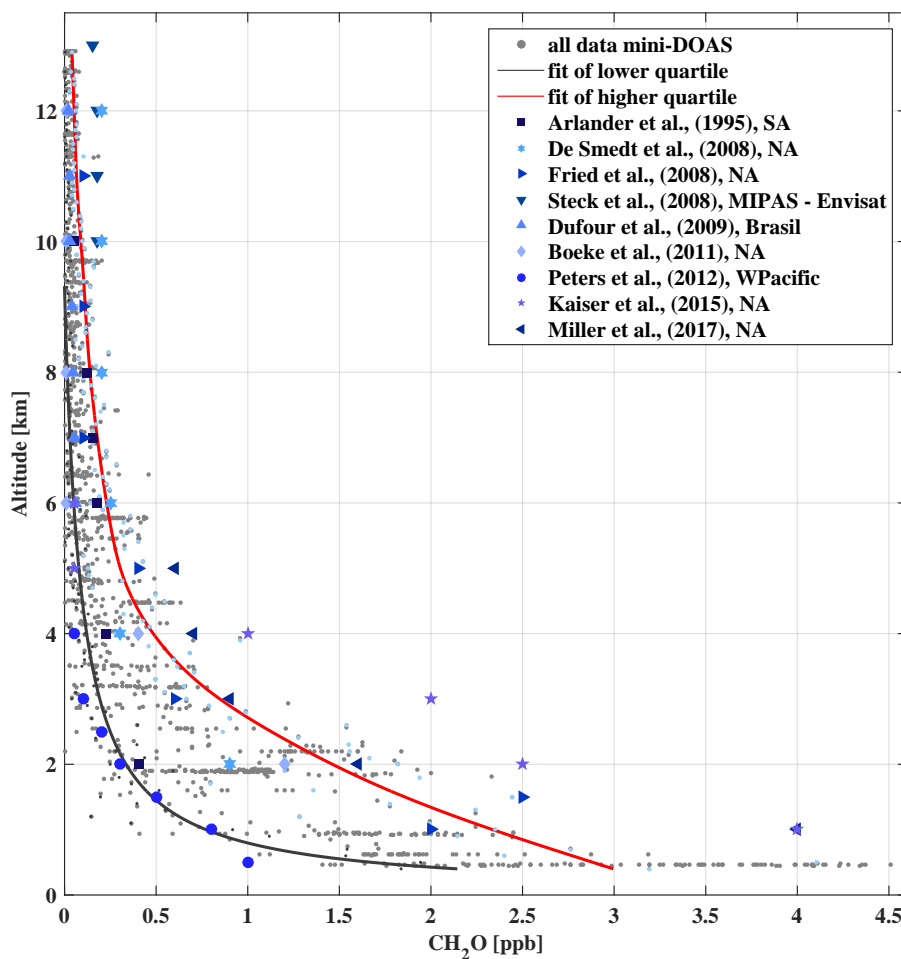


Figure 10. Comparison of different CH_2O measurements available from the literature (Arlander et al., 1995; De Smedt et al., 2008a; Fried et al., 2008; Dufour et al., 2009; Steck et al., 2008; Boeke et al., 2011; Peters et al., 2012; Kaiser et al., 2015; Chan Miller et al., 2017) with those of the present study (black). The geographical regions of the measurements are Brazil, South America (SA), North America (NA), West Pacific (WPacific) and MIPAS-Envisat measurements covering orbit 8164, $14^\circ \text{ S}/46^\circ \text{ W}$.

comparison, it is remarkable that the lowest CH_2O mixing ratios measured over the Amazon approximately agree with CH_2O measured within the boundary layer and middle troposphere over the West Pacific by Peters et al. (2012). Our measurements in the upper troposphere compare well to findings from Dufour et al. (2009) and Boeke et al. (2011) over Brazil and North America, respectively. The lowest mixing ratios measured in the middle and upper troposphere may reflect CH_2O formed during the oxidation of mostly CH_4 and, if available, some residual VOCs, OVOCs, and BVOCs (cf., see fig. 9, panel (c) for $\text{C}_2\text{H}_2\text{O}_2$ and panel (d) for $\text{C}_3\text{H}_4\text{O}_2^*$), since their heterogeneous removal is certainly slower than the CH_2O photochemical lifetime of only a few hours (Frost et al., 2002). In contrast, the largest CH_2O mixing ratios measured over the Amazon at any altitude appear slightly smaller than the average, and significantly smaller than the maximum mixing ratios reported from



the joint SENEX aircraft observations of CH_2O and $\text{C}_2\text{H}_2\text{O}_2$ over North America (Kaiser et al. (2015); Chan Miller et al. 315 (2017)).

$\text{C}_2\text{H}_2\text{O}_2$ mixing ratios range from 85 ppt to 250 ppt below 500 m altitude and decrease in the upper troposphere (12–14 km) to mixing ratios from 5 ppt (our detection limit) to about 49 ppt. Close to the ground, our results are comparable to $\text{C}_2\text{H}_2\text{O}_2$ mixing ratios found over North America by Kaiser et al. (2015) and Chan Miller et al. (2017), but much larger than those measured in pristine air masses of the South Pacific (7–23 ppt) by Lawson et al. (2015). Evidently, besides the 320 $\text{C}_2\text{H}_2\text{O}_2$ formation during the oxidation of BVOCs (Wennberg et al., 2018), a fraction of the near surface and boundary layer $\text{C}_2\text{H}_2\text{O}_2$ is certainly due to direct emission by biomass burning (Zarzana et al., 2018; Andreae, 2019). In the middle troposphere, our inferred mixing ratios of $\text{C}_2\text{H}_2\text{O}_2$ are significantly larger than observations during SENEX (which reach to approximately 6 km altitude) and are also larger in the upper troposphere above 6 km when comparing to data extrapolated from SENEX. Between 6 and 14 km altitude, $\text{C}_2\text{H}_2\text{O}_2$ enhancements of up to ≈ 63 ppt become apparent when compared to 325 either the SENEX data or the binned lower quartile of our data. Such elevated mixing ratios of $\text{C}_2\text{H}_2\text{O}_2$ in the middle and upper troposphere point to an efficient vertical transport of $\text{C}_2\text{H}_2\text{O}_2$ and its precursors VOCs, OVOCs, and BVOCs from their emission sources at the ground (Andreae et al., 2001). Further, $\text{C}_2\text{H}_2\text{O}_2$ (and $\text{C}_3\text{H}_4\text{O}_2^*$) present at higher atmospheric altitudes may serve as a marker for the formation of ISOPOO (isoprene peroxy radicals), ISOPOOH (oligomer hydroxyhydroperoxides) and finally IEPOX (isoprene epoxydiols) within the isoprene oxidation chain (Wennberg et al., 2018). In fact, IEPOX mediated 330 SOA formation in the upper troposphere over the Amazon has been reported from observations made within the framework of the ACRIDICON-CHUVA project (Andreae et al., 2018; Schulz et al., 2018).

The detection of $\text{C}_3\text{H}_4\text{O}_2^*$, here taken as the sum of methylglyoxal and larger carbonyls as described previously, appears elusive due to the spectral interference among the different species. Weighting of the measured total absorption for $\text{C}_3\text{H}_4\text{O}_2^*$ with the relative absorption cross sections of the inferred $\text{C}_3\text{H}_4\text{O}_2$, $\text{C}_4\text{H}_6\text{O}_2$ (biacetyl), and $\text{C}_4\text{C}_8\text{O}_4$ (acetylpropionyl) (Zarzana 335 et al. (2017), fig. S4) may be indicative of the relative abundance of each species. As in Zarzana et al. (2017), we recommend a weighting factor of 2.0 ± 0.5 by which the inferred $\text{C}_3\text{H}_4\text{O}_2^*$ needs to be divided for indicative $\text{C}_3\text{H}_4\text{O}_2$ mixing ratios.

Due to the lack of previous atmospheric $\text{C}_3\text{H}_4\text{O}_2^*$ (or $\text{C}_3\text{H}_4\text{O}_2$) measurements, it is more difficult to validate our inferred $\text{C}_3\text{H}_4\text{O}_2^*$ profile (fig. 9, panel (d)). As for the other measured hydrocarbons, the largest $\text{C}_3\text{H}_4\text{O}_2^*$ mixing ratios between 1.2 ppb and 2.8 ppb (mean $[\text{C}_3\text{H}_4\text{O}_2^*]=1.6$ ppb) are found near the ground and within the planetary boundary layer. Below 1 km 340 altitude, our results of 0.8 ppb to 2.8 ppb (mean $[\text{C}_3\text{H}_4\text{O}_2^*]=1.5$ ppb) are considerably larger than recently reported $\text{C}_3\text{H}_4\text{O}_2$ mixing ratios (28 ppt to 365 ppt) from a Mediterranean site with intense biogenic emissions and low levels of anthropogenic trace gases (Michoud et al., 2018), as well as measurements at Cape Grim (28 ± 11 ppt) and the Chatham Rise (10 ± 10 ppt) in pristine marine air (Lawson et al., 2015). Therefore, we expect a major fraction of the enhanced $\text{C}_3\text{H}_4\text{O}_2^*$ to be related to the oxidation of BVOCs and biomass burning (e.g., Andreae and Merlet (2001); Akagi et al. (2011); Stockwell et al. (2015); 345 Zarzana et al. (2017, 2018); Andreae (2019)). Evidence that the former is overall the more relevant process (as compared to direct emissions by biomass burning) in the Amazonian troposphere is also provided by the relatively compact clustering of the inferred $\text{C}_3\text{H}_4\text{O}_2^*$ along the fit of the lower quartile of the data.



5 Discussion

5.1 Vertical profiles and precursor VOCs

350 Above the boundary layer, significant enhancements in $C_2H_2O_2$ and $C_3H_4O_2^*$ mixing ratios above the inferred backgrounds are observed (fig. 9, panels (c) and (d)). After applying a correction factor of 2.0 ± 0.5 to the measured $C_3H_4O_2^*$ mixing ratios as discussed above, methylglyoxal exceeds the inferred glyoxal mixing ratios by up to a factor of five for all measurements. Because of many long flight sections above the remote rain forest, which were to our knowledge at least partly free of fires and plumes, as well as the comparatively different shape of the formaldehyde profile, not all of these enhancements can be
355 attributed to direct emissions from biomass burning.

As their dominant source, isoprene globally accounts for 67 %, 47 %, and 79 % of the yearly emissions of formaldehyde, glyoxal, and methylglyoxal (Fu et al., 2008), respectively, leading to their generally correlated vertical profiles. As argued by Fu et al. (2008) and Fu et al. (2019), the oxidation of isoprene under low NO_x conditions may be delayed by hours or even several days. This prolonged lifetime combined with the efficient vertical atmospheric transport in the tropics leads to
360 isoprene oxidation above the boundary layer. As a consequence, we suspect the in situ formation of glyoxal and methylglyoxal and finally formaldehyde from isoprene oxidation to lead to the observed enhanced mixing ratios in the free troposphere. The methylglyoxal enhancements in the middle troposphere are approximately five times larger than the observed glyoxal mixing ratios. Molar yields of glyoxal and methylglyoxal from second and third generation isoprene oxidation combined, are 6.2 % and 34 %, respectively (Fu et al., 2008). Therefore, we expect the in situ formation of methylglyoxal from isoprene oxidation
365 to be approximately five times larger than the respective glyoxal production. In accordance with our measurements, this should lead to five times larger methylglyoxal mixing ratios compared to glyoxal in the free troposphere.

Despite their common dominant precursor, the secondary sources of the gases are different (PAN for formaldehyde, acetylene for glyoxal, and acetone for methylglyoxal (Fu et al., 2008)), and might therefore differently contribute to our measurements. While acetylene is mostly an anthropogenic emitted trace, acetone additionally has direct biogenic sources. Both gases have a
370 long lifetime of up to 18 and 22 days, respectively (Fu et al., 2008). Therefore, vertically transported acetylene from ground-based combustion processes might be a further source of the observed glyoxal production in the free troposphere. While acetone is also emitted in biomass burning processes (one fifth of the total acetone budget (Pöschl et al., 2001)), an equally large source of acetone emissions is decomposing plant material (10^{-4} g g^{-1} (Warneke et al., 1999)). The remaining acetone is to a large part an oxidation product of hydrocarbons and also an oxidation product of isoprene under low NO_x conditions, which are
375 typical for rain forests (Warneke et al., 2001). Mean acetone mixing ratios in the boundary layer above tropical rain forests are on the order of 2 nmol mol^{-1} (Pöschl et al., 2001). Besides isoprene oxidation, a fraction of the observed methylglyoxal enhancements in the free troposphere might therefore be a direct or secondary (through the oxidation of hydroacetone) product of acetone oxidation above the boundary layer.

It is remarkable, that even though formaldehyde, glyoxal, and methylglyoxal have a common dominant source (isoprene)
380 and sink (photolysis), the relative profile shapes are different. Especially above the boundary layer, the inferred formaldehyde mixing ratios decrease faster with increasing altitude than the vertical profiles of glyoxal and methylglyoxal do (fig. 9, panel

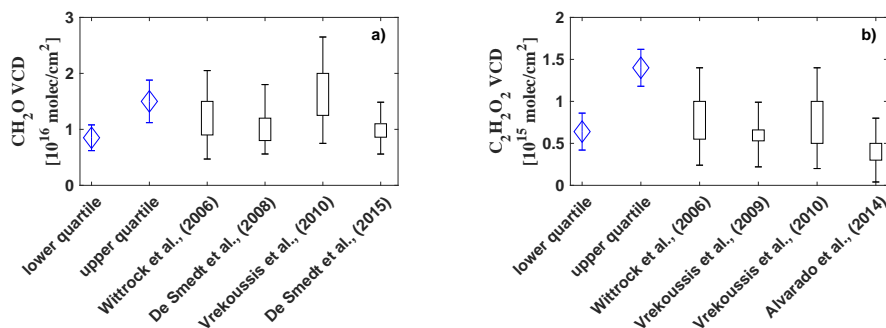


Figure 11. Comparison of the integrated total column amounts of CH₂O and C₂H₂O₂. The vertical bars indicate the range of the observed vertical column amounts as reported in the respective studies. The uncertainty range for Wittrock et al. (2006) and Alvarado et al. (2014) was estimated based on Vrekoussis et al. (2009).

(b)). It is thus to question whether the relative contribution to the total sink of photolysis and reactions with OH radicals in a low-NO_x, high-VOC, and low-HO_x environment or the different efficiencies regarding the uptake into aerosols or cloud particles may alter the relative profile shapes of the three species. The water solubility of the gases is largely different ($H^{CP} = 32$ mol m⁻³ Pa⁻¹ for formaldehyde, $H^{CP} = 4100$ mol m⁻³ Pa⁻¹ for glyoxal, and $H^{CP} = 370$ mol m⁻³ Pa⁻¹ for methylglyoxal, see Sander (2015)) and significantly smaller for formaldehyde than glyoxal. Heterogeneous uptake may therefore not provide an explanation for the relative depletion of formaldehyde over glyoxal and methylglyoxal in the middle troposphere.

5.2 Comparison with satellite measurements

As neither CH₂O nor C₂H₂O₂ have relevant stratospheric sources, the integration of the profiles yields their total vertical column density (VCD). The uncertainty of the integrated profiles follows from the altitude weighted total error of our measurements as displayed in fig. 4. We compare our findings to measurements from GOME (Global Ozone Monitoring Experiment), SCIAMACHY (SCanning Imaging Absorption spectrometer for Atmospheric CHartography), OMI (Ozone Monitoring Instrument), and GOME-2, which combined provide global CH₂O and C₂H₂O₂ observations covering more than a decade (fig. 11).

Integration of the CH₂O profiles yields total column amounts of $(0.9 \pm 0.2) \cdot 10^{16}$ molec cm⁻² (lower quartile as plotted in fig. 9) to $(1.5 \pm 0.4) \cdot 10^{16}$ molec cm⁻² (upper quartile), with a mean of $(1.1 \pm 0.3) \cdot 10^{16}$ molec cm⁻² (all data, fig. 11, a). Satellite observations generally report enhanced CH₂O VCDs over regions with large biogenic emissions, especially over the Amazon Basin, with maximal enhancements during the dry season. Monthly means of CH₂O VCDs measured by GOME and SCIAMACHY in the years 1996–2007 over the Amazon report maximal enhancements of $1\text{--}2 \cdot 10^{16}$ molec cm⁻² during the dry season and much smaller vertical column densities of $0.8 \cdot 10^{16}$ molec cm⁻² during the wet season (De Smedt et al., 2008b). Our inferred CH₂O vertical column densities based on the lower quartile agree well with their measurements during the wet season, while our integrated profile of the upper quartile lies within the observations during the dry season. Our results agree equally well with SCIAMACHY observations in 2005 over South America with an annual mean CH₂O VCD



of approximately $1.2 \cdot 10^{16}$ molec cm^{-2} as reported by Wittrock et al. (2006) and also agree with GOME-2 observations, for
405 which Vrekoussis et al. (2010) report CH_2O VCDs of 1.2 to $1.6 \cdot 10^{16}$ molec cm^{-2} over the Amazon Basin for the years
2007 to 2008. Finally, yearly averaged CH_2O from OMI and GOME-2 observations over Brazil between 2007 and 2013 by
De Smedt et al. (2015) agree with our mean of $1.1 \cdot 10^{16}$ molec cm^{-2} .

The integrated $\text{C}_2\text{H}_2\text{O}_2$ profiles range from $(0.6 \pm 0.2) \cdot 10^{15}$ molec cm^{-2} (lower quartile) to $(1.4 \pm 0.4) \cdot 10^{15}$ molec cm^{-2}
(upper quartile), with a mean of $(1.0 \pm 0.3) \cdot 10^{15}$ molec cm^{-2} . Based on SCIAMACHY measurements in the years 2002 to
410 2007, Vrekoussis et al. (2009) report seasonal mean $\text{C}_2\text{H}_2\text{O}_2$ VCDs of $0.5 \cdot 10^{15}$ molec cm^{-2} over northern South America
in autumn (fig. 11, b). In good agreement with our lower limit, Wittrock et al. (2006) report slightly higher SCIAMACHY
 $\text{C}_2\text{H}_2\text{O}_2$ observations of approximately $0.6\text{--}0.7 \cdot 10^{15}$ molec cm^{-2} over North Brazil for the year 2005. Corresponding to our
mean VCD, Vrekoussis et al. (2010) further report average VCDs of $0.5 \cdot 10^{15}$ molec cm^{-2} with maximal enhancements of
 $1 \cdot 10^{15}$ molec cm^{-2} based on GOME-2 measurements over South America in the years 2007 to 2008. Observations from OMI
415 yield slightly lower monthly mean $\text{C}_2\text{H}_2\text{O}_2$ VCDs of $0.3 \cdot 10^{15}$ molec cm^{-2} (Alvarado et al., 2014). The VCD based on the
upper quartile, which is indicative of the large amount of direct glyoxal emissions from various biomass burnings into the
boundary layer, is larger than, but still within the uncertainty range of the SCIAMACHY and GOME-2 observations.

5.3 R_{XF}^* above the Amazon rain forest

As outlined above, the different air masses probed with the mini-DOAS and AMTEX instrument prevent a definition of emis-
420 sion ratios relative to CO (sect. 2.1 and 2.2). Instead, we infer the emission ratios R_{GF}^* and R_{MF}^* relative to CH_2O , as often
done in remote sensing studies (Fu et al. (2008); Kaiser et al. (2015); Stavrou et al. (2016); Zarzana et al. (2017, 2018), and
others). According to the literature, the background uncorrected emission ratio is defined as

$$R_{\text{XF}}^* = \frac{[\text{X}]}{[\text{CH}_2\text{O}]}. \quad (3)$$

In this study, [X] is either $[\text{C}_2\text{H}_2\text{O}_2]$ or $[\text{C}_3\text{H}_4\text{O}_2^*]$, as often used in satellite and modelling studies related to hydrocarbon
425 precursors of the studied species (Fu et al. (2008); Kaiser et al. (2015), and others). R_{XF}^* is calculated for each measurement
and analysed with respect to the measurement altitude (fig. 12, panel (a) and (b)).

5.3.1 R_{GF}^*

R_{GF}^* mostly remains smaller than 1.0, with a total mean of $\bar{R}_{\text{GF}}^* = 0.35$, but reaches maximum values > 5.0 during several
measurements. Small ratios < 0.05 and large ratios > 1.0 can be observed throughout all analysed flights and nearly all altitudes.
430 The comparison with Kaiser et al. (2015) shows, that the inferred R_{GF}^* is notably larger than during most of their measurements
over the south-eastern US. Our results are in much better agreement with the R_{GF}^* MacDonald et al. (2012) inferred during
measurements over an Asian rain forest. Their R_{GF}^* in the range 0.2 to 0.7 agrees with most of our measurements as well
as with \bar{R}_{GF}^* of approximately 0.35. From measurements above the Kisatchie National Forest and the Mark Twain National
Forest in the south-eastern US, Kaiser et al. (2015) conclude characteristically low R_{GF}^* in pristine regions with strong isoprene
435 emissions, while regimes dominated by monoterpene emissions appear to have higher R_{GF}^* . Most of our measurements took

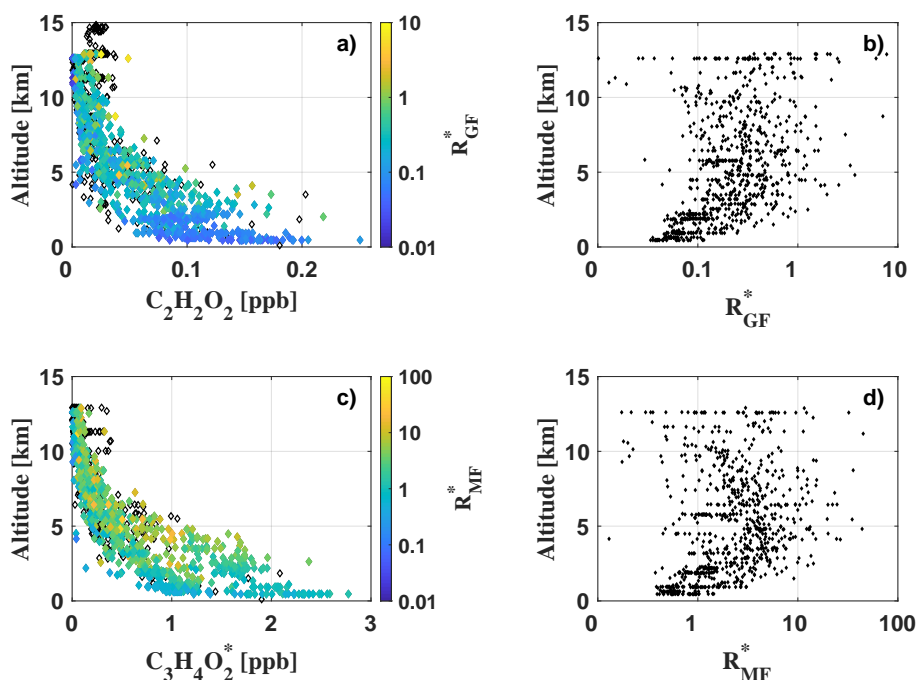


Figure 12. Vertical profiles of $C_2H_2O_2$ (panel (a)) and $C_3H_4O_2^*$ (panel (c)), colour-coded by the ratios R_{GF}^* and R_{MF}^* , respectively, for each measurement during flights AC09, AC11, AC12, and AC13. Black diamonds indicate measurements with missing CH_2O data (recorded with a different spectrometer) and consequently missing ratios. Panels (b) and (d) illustrate the vertical profiles of R_{GF}^* and R_{MF}^* throughout the troposphere. For panels (b) and (d) a logarithmic x-axis has been chosen for a better illustration of the altitude dependence of small R_{GF}^* and R_{MF}^* , respectively.

place in pristine air masses above the rain forest and far away from any major population centre or other anthropogenic emission sources. Monoterpene and isoprene emissions over the central Amazon were studied in multiple investigations (e.g. Helmig et al. (1998) and Kesselmeier et al. (2000)). All these studies reported generally low mixing ratios of monoterpenes compared to isoprene, which composes 90 % of the total VOC budget in the Amazon (Kuhn et al., 2007). Emissions of monoterpenes, like α -pinene, on the other hand, are at least one order of magnitude smaller. Approximately the same relation was found for the total monoterpene emissions (Kuhn et al., 2007; Rizzo et al., 2010). Kaiser et al. (2015) report on approximately 1.2–2.0 times larger $C_2H_2O_2$ yield from α - and β -pinene oxidation with respect to CH_2O . Still, the significant predominance of isoprene emissions over the Amazon clearly compensate for this effect. We conclude that isoprene and not monoterpenes is the dominant precursor of CH_2O and $C_2H_2O_2$ for our observations. Contrary to the measurements of Kaiser et al. (2015) in isoprene rich regimes, the results indicate significantly elevated R_{GF}^* in the troposphere over the Amazon. This is a direct consequence of the much lower CH_2O mixing ratios as compared to their measurements over the south-eastern US. CH_2O generally does not exceed 1–2 ppb (except for direct measurements in biomass burning or in the Manaus city plume), which is four times less than reported by Kaiser et al. (2015) for pristine air masses over the Mark Twain National Forest (ca. 8 ppb).



Our $C_2H_2O_2$ mixing ratios, on the other hand, are comparable to their findings and typically 100 ppt in the lower troposphere.
450 As a result, we obtain significantly higher R_{GF}^* than Kaiser et al. (2015) for the pristine troposphere.

Based on the SENEX observations, Chan Miller et al. (2017) reported mean R_{GF}^* of 0.024 below 1 km altitude. Interestingly, Chan Miller et al. (2017) obtained larger R_{GF} of up to 0.06 when NO_x was very low (0.1–0.5 ppb). Even though we are not able to infer NO_x concentrations for all measurements due to instrument failures, we were able to measure NO_2 during all analysed flights. Inferred NO_2 mixing ratios from mini-DOAS measurements were very low during all flights. Mixing ratios
455 above 1 ppb were inferred only in rare cases and exclusively over direct emission sources like Manaus city and in biomass fire plumes. We conclude from these overall low NO_2 mixing ratios, that the measurements during the campaign were generally under very low NO_x conditions. As described in detail by Chan Miller et al. (2017), this could lead to prompt glyoxal formation through isoprene peroxy radicals and thus slightly enhanced R_{GF} compared to observations under high NO_x . Further, from our measurements over Manaus city, we cannot detect any sizeable influence of anthropogenic VOCs on the inferred R_{GF}^* . During
460 several low overpasses of the city (< 2 km flight altitude), R_{GF}^* did not show any significant difference to measurements distant from anthropogenic emission sources. During the measurements in the city plume, the relative increase of CH_2O and $C_2H_2O_2$ mixing ratios was similar, leading to consistent R_{GF}^* .

Finally, the vertical profile of R_{GF}^* indicates slightly elevated ratios above the boundary layer and in the free troposphere (fig. 12, panel (b)). Within the boundary layer, R_{GF}^* remains approximately constant. Both features were previously observed
465 by Kaiser et al. (2015) up to 6 km, however less pronounced. Above 10 km, our results indicate a slight decrease of R_{GF}^* . When discussing these observations, one has to keep in mind the very low CH_2O and $C_2H_2O_2$ concentrations in the upper troposphere and the increasing influence of noise on the inferred mixing ratios. Above 6 km, we observe mean CH_2O and $C_2H_2O_2$ of only 54 ± 40 ppt and 15 ± 5 ppt, respectively. Still, the increase in R_{GF}^* between ~ 2 –10 km appears most pronounced right above the boundary layer at 2 km, where CH_2O and $C_2H_2O_2$ mixing ratios are still significantly above the
470 detection limits. Notably, the correlation of $C_2H_2O_2$ and CH_2O is higher within the boundary layer. In the free troposphere, R_{GF}^* varies on average by 60 % among the different measurements in the same altitude range. Following the argumentation of Kaiser et al. (2015), this behaviour can be attributed to the uniform mixing of CH_2O and $C_2H_2O_2$ within the boundary layer.

5.3.2 R_{MF}^*

Generally, R_{MF}^* appears approximately 10 times larger than R_{GF}^* (fig. 12, panels (c) and (d)). $R_{MF}^* < 1$ are observed only
475 for a minority of the measurements and mostly for background $C_3H_4O_2^*$ concentrations. Larger $R_{MF}^* > 1$ are inferred at all altitudes, with a total mean $\overline{R_{MF}^*} = 3.6$ and a maximum ratio $R_{MF,max}^* = 47$. As discussed above for R_{GF}^* , the vertical profile of R_{MF}^* indicates slightly larger R_{MF}^* above the boundary layer and throughout the free troposphere. In the upper troposphere, R_{MF}^* decreases again, leading to a concave curvature of the vertical profile for small R_{MF}^* , as previously described for R_{GF}^* . Several studies were published on the emission ratio of $C_3H_4O_2$ to CH_2O (or CO) in biomass burning plumes (e.g. Hays
480 et al. (2002); Müller et al. (2016); Zarzana et al. (2017, 2018)). To our knowledge, comparable data for air masses of the free troposphere are still missing. As a result, we cannot thoroughly compare R_{MF}^* to other findings, but focus our analysis on measurements within biomass burning plumes.



5.4 Normalised excess mixing ratios in biomass burning plumes and inferred emission factors

During the four measurement flights, a total of twelve biomass burning plume intercepts were identified based on video imagery (e.g. fig. 7 for events AC11-1.1/1.2 and AC11-3.1/3.2). Most of the plume measurements occurred south of Manaus, and during two extensive flight periods of AC11 and AC13 at altitudes below 2 km. The precise location of all plume intercepts during flight AC11, and the related horizontal averaging kernels of the telescopes are given in fig. 6. As indicated by the backward trajectories, three hours prior to detection all probed air masses moved well within the boundary layer, below 600 m altitude. This time frame more than covers the atmospheric lifetimes of CH_2O , $\text{C}_2\text{H}_2\text{O}_2$ and $\text{C}_3\text{H}_4\text{O}_2$. Consequently, the measured mixing ratios of these gases are a result of fresh emissions at the surface. Each biomass burning plume encounter correlates with significant enhancements in CH_2O , $\text{C}_2\text{H}_2\text{O}_2$ and $\text{C}_3\text{H}_4\text{O}_2$ over the background by 13 to 400 %. Based on the backward trajectories combined with video imagery and the short lifetimes of the gases, contributions from other major emission sources (e.g. Manaus city) can largely be excluded. The exact timing, location and altitude of each plume intercept is given in Table 3. As indicated by the numbering in column 1, some of the plumes were probed more than once, giving a total of eight different biomass burning plumes with 12 encounters (further on called events AC11-1.1 to AC13-5). Based on fig. 9, the mean background mixing ratio of each gas is subtracted from the measured mixing ratios within the plumes. From the resulting enhancements, the normalized excess mixing ratio R_{XF} (or NEMR) is calculated according to

$$R_{\text{XF}} = \frac{\Delta[X]}{\Delta[\text{CH}_2\text{O}]} = \frac{[X_{\text{fire}}] - [X_{\text{bkg}}]}{[\text{CH}_2\text{O}_{\text{fire}}] - [\text{CH}_2\text{O}_{\text{bkg}}]} \quad (4)$$

with X being either $\text{C}_2\text{H}_2\text{O}_2$ or $\text{C}_3\text{H}_4\text{O}_2^*$. The results for each individual biomass burning event as well as the mean and range of R_{GF} and R_{MF} are given in Table 3.

5.4.1 R_{GF}

R_{GF} ranges between 0.024 and 0.112, with an average of $\overline{R_{\text{GF}}} = 0.065 \pm 0.048$. Repeated measurements of the same biomass burning plumes all agree well within the error, indicating the respective plumes were in fact the major emission sources throughout the measurements. The plume AC11-3 (fig. 7) yields the highest R_{GF} of 0.097 and 0.112. Unfortunately, the plume was not reported in the MODIS fire database. Therefore, we do not know the precise location of the fire and cannot discuss the results with respect to the distance of the aircraft from the plume. The smallest R_{GF} of 0.024 is found during a measurement with an approximately 1000 m higher flight altitude than during the rest of the events.

Our results are consistent with recent laboratory studies on biomass burning emissions by Zarzana et al. (2018) as well as different field measurements and satellite observations by Chan Miller et al. (2014, 2017); DiGangi et al. (2012); Wittrock et al. (2006) and Zarzana et al. (2017). From laboratory measurements, Zarzana et al. (2018) reported an average R_{GF} of 0.068 for fresh emissions and different kinds of fuels. Without further knowledge on the fuels burned during the observed events, we cannot make firm conclusions on the photochemistry within the fire plumes. While different fuel types may lead to changing emission factors of glyoxal, Zarzana et al. (2018) observed only little variance in R_{GF} for different burning species. The correlation of $\text{C}_2\text{H}_2\text{O}_2$ and CH_2O seems to be consistent for different kinds of fuel. The lack of knowledge of the exact



Table 3. Inferred normalised excess mixing ratios and emission factors for individual biomass burning events (range and mean). R_{GF} and R_{MF} are given in mole mole⁻¹. The emission factors EF_G and EF_M are in units of g kg⁻¹.

event	time interval [UTC]	location	altitude [km]	R_{GF}	R_{MF}	EF_G	EF_M
AC11-1.1	15:03:19–15:03:51	2.9° S, 60.1° W	0.624–0.632	0.05 ± 0.03	0.09 ± 0.13	0.23 ± 0.13	0.50 ± 0.76
AC11-1.2	15:03:48–15:04:16	2.9° S, 60.1° W	0.615–0.647	0.03 ± 0.02	0.11 ± 0.16	0.16 ± 0.12	0.65 ± 0.94
AC11-2.1	17:21:06–17:23:31	3.6° S, 60.3° W	0.455–0.471	0.06 ± 0.04	0.86 ± 0.39	0.26 ± 0.19	4.96 ± 2.6
AC11-2.2	17:23:31–17:24:48	3.6° S, 60.3° W	0.453–0.470	0.06 ± 0.04	0.66 ± 0.31	0.26 ± 0.18	3.8 ± 2.04
AC11-2.3	17:24:50–17:26:30	3.6° S, 60.3° W	0.452–0.470	0.03 ± 0.03	0.51 ± 0.26	0.16 ± 0.15	2.93 ± 1.68
AC11-3.1	17:43:27–17:44:41	2.9° S, 60.5° W	0.450–0.456	0.11 ± 0.10	1.50 ± 0.60	0.52 ± 0.47	8.64 ± 4.13
AC11-3.2	17:44:43–17:45:52	2.8° S, 60.5° W	0.449–0.454	0.10 ± 0.11	1.30 ± 0.70	0.45 ± 0.52	7.49 ± 4.49
AC13-1	16:33:41–16:34:20	11.0° S, 56.2° W	0.923–0.934	0.04 ± 0.05	1.20 ± 0.60	0.18 ± 0.23	6.91 ± 3.90
AC13-2	16:34:20–16:34:56	11.1° S, 56.2° W	0.921–0.932	0.08 ± 0.07	1.40 ± 0.70	0.37 ± 0.34	8.06 ± 4.55
AC13-3	16:35:39–16:36:18	11.2° S, 56.2° W	0.918–0.929	0.03 ± 0.04	0.76 ± 0.43	0.13 ± 0.17	4.35 ± 2.73
AC13-4	16:37:01–16:37:43	11.2° S, 56.2° W	0.915–0.932	0.05 ± 0.04	0.81 ± 0.43	0.23 ± 0.19	4.67 ± 2.76
AC13-5	16:52:15–16:53:03	11.2° S, 56.2° W	1.849–1.191	0.02 ± 0.02	0.56 ± 0.27	0.11 ± 0.10	3.25 ± 1.77
Range				0.02–0.11	0.09–1.50	0.11–0.52	0.50–8.64
Mean				0.07 ± 0.05	0.98 ± 0.42	0.25 ± 0.23	4.70 ± 2.70

515 fuels burned in each fire is therefore not an issue when comparing R_{GF} of the different plumes and intercepts. In two older studies, Hays et al. (2002) and McDonald et al. (2000b) report much higher R_{GF} on the order of approximately 2.5 to 3 for *Palmae* and *Poaceae* (Hays et al., 2002) and even up to 4 (McDonald et al., 2000b). Our inferred R_{GF} are at least one order of magnitude lower. In fact, results larger than 1 are only observed for the background-uncorrected R_{GF}^* in the free troposphere.

520 During recent field measurements over the US, Zarzana et al. (2017) report R_{GF} in the range 0.008 to 0.110. Due to the very nature of airborne plume measurements, we do not know by how much the measurements differ with respect to plume age, air mass origin, atmospheric composition, measurement distance to the plume, etc. Despite the very different atmospheric backgrounds and conditions, our measurements over the rain forest agree well with their findings.

525 Measurements of an aged biomass burning plume yield slightly smaller R_{GF} of 0.02 to 0.03 (DiGangi et al., 2012). Of all events, event AC13-5 is most likely the oldest plume measured. This is a consequence of the high flight altitude in combination with the distance from the aircraft to the plume during the measurement. AC13-5 has the smallest R_{GF} of only 0.024, which agrees with the findings of DiGangi et al. (2012). We cannot state by how much this plume measurement is influenced by the general atmospheric background. The air masses in the boundary layer are generally highly polluted with biomass burning emission of different ages. We do not know how much these differently aged emissions influenced our individual plume measurements. Therefore, we cannot draw a distinct relationship between R_{GF} and the plume ages, which, due to the well-
530 mixed condition of the boundary layer most probably varied between several minutes to hours during all measurements.



5.4.2 R_{MF}

R_{MF} ranges between 0.09 and 1.50, with an average of $\bar{R}_{MF} = (0.98 \pm 0.42)$. Three of the eight probed plumes yield $R_{MF} > 1$ (both measurements of AC11-3, AC13-1, and AC13-2). All the other plumes yield $R_{MF} < 1$, in the range of 0.09 to 0.86. For event AC11-1, R_{GF} is comparable to the other results, while R_{MF} is significantly smaller than the average \bar{R}_{MF} by approximately a factor of 10. Based on the video imagery, the size of the observed plumes as well as the estimated distance to the aircraft are comparable during events AC11-1 and AC11-3 (fig. 7). Still, they yield very different normalised excess mixing ratios. In fact, the largest R_{MF} and R_{GF} are obtained during event AC11-3. Accordingly, the emission of $C_2H_2O_2$ and $C_3H_4O_2^*$ with respect to CH_2O is the highest within this biomass burning plume. Interestingly, this is not connected to the size and quantity of the biomass burning events seen by the telescopes. The highest emissions (i.e. the largest plumes) were observed during event AC11-2, where three different large fires were simultaneously detected in a generally hazy atmosphere rich in fresh emissions (fig. 7). These plumes were also recorded by MCD14 on MODIS (fig. 6, red dots in the field of view of event 2.2). Laboratory measurements report R_{MF} approximately between 1 and 2 for different kinds of fuels (Hays et al., 2002). This is the upper range of our observations. Instead of R_{MF} , Zarzana et al. (2018) report the ratio $C_3H_4O_2$ to $C_2H_2O_2$ (R_{MG}) to be on the order of 1.7–2.5 for burning rice straw and different kinds of canopy. Our measurements yield R_{MG} in the range 1–3, with the exception of event AC11-1, where $R_{MG} < 1$ due to the small $C_3H_4O_2^*$ mixing ratios. Event AC11-3 yields $R_{MG}=1$ during both measurements. This reflects the correlated strong enhancement of both gases within the biomass burning plumes.

5.4.3 Biomass burning emission factors

According to Andreae (2019), the biomass burning emission factors for $C_2H_2O_2$ and $C_3H_4O_2^*$ are defined by the normalised excess mixing ratio R_{XF} as

$$EF_X = R_{XF} \frac{MW_X}{MW_{CH_2O}} EF_{CH_2O} \quad (5)$$

using the molecular weight MW of each species, and the mean emission factor EF_{CH_2O} of the reference trace gas CH_2O . As the latter was not measured during the campaign, we use the recent comprehensive compilation by Andreae (2019), which reports EF_{CH_2O} with respect to different combustion processes and fuel types. For tropical forest fires, Andreae (2019) inferred mean $EF_{CH_2O} = 2.4 \pm 0.63$. The resulting EF_G and EF_M are listed in Table 3 for each biomass burning plume intercept in units of g (target species) kg^{-1} (fuel).

EF_G ranges from 0.11 to 0.52 g glyoxal per kg of fuel burned with a mean emission factor of $(0.25 \pm 0.23) g kg^{-1}$. According to its high R_{GF} , event AC11-3 yields the highest emission factors of 0.52 and 0.45 $g kg^{-1}$. Five out of the twelve plume encounters yield emission factors of less than 0.2 $g kg^{-1}$. Corresponding to the largest EF_G , Andreae (2019) estimated $EF_G = 0.6 g kg^{-1}$ for tropical forest fires. In the same study, glyoxal emissions from open burns of agricultural residues were estimated to be approximately 60 % lower with $EF_G = 0.23 g kg^{-1}$. All biomass burning events encountered during flight AC13 were located between 11.0–11.2° S and 56.2° W. While other parts of the measurement flight were located over rain forest,



this region is largely dominated by agricultural activities. EF_G of events AC13-1 to AC13-5 ranges from 0.11 to 0.37 g kg⁻¹. Assuming that the biomass burning plumes were dominated by agricultural residues during these measurements, we infer a corresponding mean emission factor $EF_G=0.2$ g glyoxal per kg of open burns of agricultural residues. The range of EF_G further agrees with laboratory measurements by Zarzana et al. (2018), who reported EF_G in the range of 0.06 to 0.55 g kg⁻¹ depending on the fuel type.

EF_M ranges between 0.5 and 8.64 g methylglyoxal per kg of fuel burned, with a mean emission factor of (4.68 ± 2.7) g kg⁻¹. For each biomass burning event, EF_M is at least twice as high as EF_G . The largest EF_M were found during flight AC13, i.e. for fires dominated by agricultural residues. Even after applying the correction factor of 2 on the inferred EF_M , the results are significantly larger than reported by Zarzana et al. (2018) from laboratory measurements, who found maximal emission factors of approximately 2 g kg⁻¹ for burns of duff. While their absolute EF_M are much lower, their results were equally variable with EF_M ranging from 0.11 to 2.0 g kg⁻¹.

6 Conclusions

We report on the first simultaneous measurements of CH₂O, C₂H₂O₂ and C₃H₄O₂* over remote and polluted sections of the Amazon. The measurements were performed from on board the DLR HALO aircraft during the ACRIDICON-CHUVA campaign in fall 2014 (Wendisch et al., 2016). The observations took place in the troposphere between 500 m and 15 km altitude, where air masses of different compositions were encountered. These include continental background as well as aged and fresh biomass burning plumes.

The observed formaldehyde mixing ratios in the lower and free troposphere range from those previously reported over the remote Pacific (Peters et al., 2012) up to those measured over continental North and South America (Kaiser et al., 2015). The lower quartile of the measured mixing ratios appears to result from the oxidation of VOCs (mostly isoprene). In the lower troposphere, enhanced formaldehyde mixing ratios have two major contributions: direct emission from biogenic sources or biomass burning and secondary formation during the degradation of short-lived VOCs. In the middle and upper troposphere, formaldehyde seems to have more constant sources and sinks than in the lower troposphere. While the sink (mostly photolysis) may not vary significantly with altitude, the degradation of longer lived VOCs provides a comparably constant source. When integrating our profiles, our observations are in good agreement with previously inferred formaldehyde VCDs from satellites (De Smedt et al., 2008b; Wittrock et al., 2006; Vrekoussis et al., 2010; De Smedt et al., 2015).

A good agreement with previous satellite measurements is also found for the lower and upper range of profile integrated glyoxal mixing ratios (Wittrock et al., 2006; Vrekoussis et al., 2009, 2010; Alvarado et al., 2014). Analogously to the presence of formaldehyde, the lower bound of glyoxal is due to the oxidation of precursor VOCs. Besides direct emissions from biomass burning and secondarily formed glyoxal from short lived precursors, the oxidation of longer lived precursors like isoprene or acetone contributes to elevated glyoxal mixing ratios in the free troposphere.

In agreement with the study of Zarzana et al. (2017), C₃H₄O₂* mixing ratios generally exceed those of glyoxal by at least a factor of 5 during the majority of the measurements. Yet, the shapes of the upper and lower bounds appear similar to the profile



shape of glyoxal in contrast to formaldehyde, which appears to decline faster above the boundary layer in the low- NO_x , high-VOC, and low- HO_x environment probed during this study. The compact clustering as well as the smooth decrease of the lower quartile mixing ratios with altitude indicate the type and sink of the precursor molecules. Apparently, these precursors should have lifetimes of at least several days, and should either be constantly emitted by the biosphere (e.g. isoprene and acetone) or occasionally during biomass burning (e.g. acetylene) before being vertically transported. R_{GF}^* and R_{MF}^* are found to increase with altitude due to the more rapid decrease of formaldehyde relative to glyoxal and methylglyoxal mixing ratios. Again, this behaviour expresses the different and changing fractions of the short and long-lived precursors relevant for the formation of formaldehyde as compared to those of glyoxal and methylglyoxal. In particular, the increasing R_{GF} and R_{MF} in the middle and upper troposphere require significant sources for both gases which are supposed to result from the oxidation of longer-lived VOCs (Schulz et al., 2018). In fact, since both gases are known to contribute to SOA formation, the elevated mixing ratios of glyoxal and methylglyoxal in the upper troposphere further lend support to the proposed SOA formation from products of isoprene oxidation as observed by Schulz et al. (2018); Andreae et al. (2018) and Williamson et al. (2019) over the Amazon Basin and generally in the tropics.

Our inferred R_{GF} in the range of 2.4–11.2 ($\overline{R}_{\text{GF}}=6.5$) for the observed biomass burning events agree well with previous studies, both in the field over North America (Zarzana et al., 2017) as well as in the laboratory fuel study (Zarzana et al., 2018). It is further in agreement with R_{GF} inferred from satellite measurements (Chan Miller et al., 2014, 2017; DiGangi et al., 2012; Wittrock et al., 2006). For R_{MF} , we infer a range of 0.09 to 1.5 with $\overline{R}_{\text{MF}}=0.98$ (or respectively smaller results when correcting the $\text{C}_3\text{H}_4\text{O}_2^*$ mixing ratios by a factor of 2.0 ± 0.5), which overlaps with the lower end of the range of normalized excess mixing ratios previously reported by Hays et al. (2002) for different types of fuels in the laboratory. The presented study as well as the measurements by Hays et al. (2002) indicate a slightly larger R_{MF} than estimated from R_{MG} and R_{GF} (appr. 0.1–0.5) reported by Zarzana et al. (2018), even though this difference may in part be a result of additional dicarbonyls included in our retrieval. In fact, when correcting R_{MF} by a factor of 2, our results agree much better to the measurements by Zarzana et al. (2018). Based on R_{GF} and R_{MF} and average emission factors for formaldehyde estimated by Andreae (2019), we infer emission factors in the range of 0.11–0.52 ($\overline{\text{EF}}_{\text{G}}=(0.25 \pm 0.23) \text{ g kg}^{-1}$) for glyoxal and 0.5–8.6 ($\overline{\text{EF}}_{\text{M}}=(4.7 \pm 2.7) \text{ g kg}^{-1}$) for methylglyoxal for the probed biomass burning events over the Amazon. Our inferred EF_{G} agrees well with the range reported from laboratory measurements (Zarzana et al., 2018). Notably, our EF_{M} is significantly larger than found in their study, also when correcting the results for possibly included additional dicarbonyls.

The presented study may be complemented by future studies with data collected during several past HALO missions, i.e. ESMVal (fall 2012), OMO (over the Mediterranean in summer 2014), EMERGe (Europe in summer 2017 and Eastern Asia in spring 2018), CAFE (over West Africa/tropical Atlantic in summer 2018), and Southtrac (Southern Argentina and northern Antarctica in fall 2019), which may provide further information on the role of carbonyls in global atmospheric chemistry.

Data availability. All the data are archived in the HALO data depository (<https://halo-db.pa.op.dlr.de/mission/5>), datasets 6495-6502 (mini-DOAS data), and 3440-3442 (AMTEX CO data). The data are accessible upon signing a data protocol.



630 *Author contributions.* TH, MK and KP operated the mini-DOAS instrument and ML and HS performed the AMTEX measurements during the ACRIDICON-CHUVA campaign. TH wrote the data retrieval software. FK performed the data analysis and wrote the paper with contributions from ML, KP and HS.

Competing interests. The authors declare that they have no conflict of interest.

635 *Financial support.* The study was funded by the German Research Foundation (DFG, HALO-SPP 1294). The contributions of FK, TH and KP were supported via the German Research Foundation (DFG) through grants PF-384/7-1, PF384/9-1, PF-384/16-1, PF-384/17, and PF-384/19. HS and ML gratefully acknowledge the support given by the DFG projects SCHL 1857/1-2, SCHL 1857/2-2, and SCHL 1857/4-1.

640 *Acknowledgements.* The authors gratefully acknowledge the NOAA Air Resources Laboratory (ARL) for the provision of the HYSPLIT transport and dispersion model and READY website (<https://www.ready.noaa.gov>) used in this publication. We acknowledge the use of imagery from the NASA Worldview application (<https://worldview.earthdata.nasa.gov/>), part of the NASA Earth Observing System Data and Information System (EOSDIS) and the use of data products and imagery from the Land, Atmosphere Near real-time Capability for EOS (LANCE) system operated by NASA's Earth Science Data and Information System (ESDIS) with funding provided by NASA Headquarters. We thank the Deutsches Zentrum für Luft- und Raumfahrt (DLR) for the support during the certification process of the mini-DOAS instrument and the DLR Flugexperimente Team at Oberpfaffenhofen, in particular, Frank Probst, Martina Hierle, Andreas Minikin and Andrea Hausold, for the support given during the ACRIDICON-CHUVA mission. We are grateful to Manfred Wendisch (University of Leipzig, Germany) for coordinating the campaign and to Steven Brown (NOAA Earth System Research Laboratory) for his helpful discussion of our measurements and conclusions.

645



References

- Akagi, S. K., Yokelson, R. J., Wiedinmyer, C., Alvarado, M. J., Reid, J. S., Karl, T., Crouse, J. D., and Wennberg, P. O.: Emission factors for open and domestic biomass burning for use in atmospheric models, *Atmospheric Chemistry and Physics*, 11, 4039–4072, <https://doi.org/10.5194/acp-11-4039-2011>, <https://www.atmos-chem-phys.net/11/4039/2011/>, 2011.
- 650 Alvarado, L., Richter, A., Vrekoussis, M., Wittrock, F., Hilboll, A., Schreier, S., and Burrows, J.: An improved glyoxal retrieval from OMI measurements, *Atmospheric Measurement Techniques*, 7, 4133, 2014.
- Amiridis, V., Marinou, E., Tsekeri, A., Wandinger, U., Schwarz, A., Giannakaki, E., Mamouri, R., Kokkalis, P., Biniotoglou, I., Solomos, S., Herekakis, T., Kazadzis, S., Gerasopoulos, E., Proestakis, E., Kottas, M., Balis, D., Papayannis, A., Kontoes, C., Kourtidis, K., Pappagiannopoulos, N., Mona, L., Pappalardo, G., Le Rille, O., and Ansmann, A.: LIVAS: a 3-D multi-wavelength aerosol/cloud database based on CALIPSO and EARLINET, *Atmospheric Chemistry and Physics*, 15, 7127–7153, <https://doi.org/10.5194/acp-15-7127-2015>, <https://www.atmos-chem-phys.net/15/7127/2015/>, 2015.
- 655 Andreae, M. and Merlet, P.: Emission of trace gases and aerosols from biomass burning, *Global Biogeochemical Cycles*, 15, 955–96, <https://doi.org/10.1029/2000GB001382>, <https://agupubs.onlinelibrary.wiley.com/doi/abs/10.1029/2000GB001382>, 2001.
- Andreae, M. O.: Emission of trace gases and aerosols from biomass burning - An updated assessment, *Atmospheric Chemistry and Physics Discussions*, 2019, 1–27, <https://doi.org/10.5194/acp-2019-303>, <https://www.atmos-chem-phys-discuss.net/acp-2019-303/>, 2019.
- 660 Andreae, M. O., Artaxo, P., Fischer, H., Freitas, S. R., Grégoire, J.-M., Hansel, A., Hoor, P., Kormann, R., Krejci, R., Lange, L., Lelieveld, J., Lindinger, W., Longo, K., Peters, W., de Reus, M., Scheeren, B., Silva Dias, M. A. F., Ström, J., van Velthoven, P. F. J., and Williams, J.: Transport of biomass burning smoke to the upper troposphere by deep convection in the equatorial region, *Geophysical Research Letters*, 28, 951–954, <https://doi.org/10.1029/2000GL012391>, <https://agupubs.onlinelibrary.wiley.com/doi/abs/10.1029/2000GL012391>, 2001.
- 665 Andreae, M. O., Afchine, A., Albrecht, R., Holanda, B. A., Artaxo, P., Barbosa, H. M., Borrmann, S., Cecchini, M. A., Costa, A., Dollner, M., et al.: Aerosol characteristics and particle production in the upper troposphere over the Amazon Basin, *Atmospheric Chemistry and Physics*, 18, 921–961, 2018.
- Arlander, D. W., Brüning, D., Schmidt, U., and Ehhalt, D. H.: The tropospheric distribution of formaldehyde during TROPOZ II, *Journal of Atmospheric Chemistry*, 22, 251–269, <https://doi.org/10.1007/BF00696637>, <https://doi.org/10.1007/BF00696637>, 1995.
- 670 Bauwens, M., Stavrakou, T., Müller, J.-F., De Smedt, I., Van Roozendael, M., van der Werf, G. R., Wiedinmyer, C., Kaiser, J. W., Sindelarova, K., and Guenther, A.: Nine years of global hydrocarbon emissions based on source inversion of OMI formaldehyde observations, *Atmospheric Chemistry and Physics*, 16, 10 133–10 158, <https://doi.org/10.5194/acp-16-10133-2016>, <https://www.atmos-chem-phys.net/16/10133/2016/>, 2016.
- Boeke, N. L., Marshall, J. D., Alvarez, S., Chance, K. V., Fried, A., Kurosu, T. P., Rappenglück, B., Richter, D., Walega, J., Weibring, P., and Millet, D. B.: Formaldehyde columns from the Ozone Monitoring Instrument: Urban versus background levels and evaluation using aircraft data and a global model, *Journal of Geophysical Research: Atmospheres*, 116, <https://doi.org/10.1029/2010JD014870>, <https://agupubs.onlinelibrary.wiley.com/doi/abs/10.1029/2010JD014870>, 2011.
- 675 Borbon, A., Ruiz, M., Bechara, J., Aumont, B., Chong, M., Huntrieser, H., Mari, C., Reeves, C. E., Scialom, G., Hamburger, T., Stark, H., Afif, C., Jambert, C., Mills, G., Schlager, H., and Perros, P. E.: Transport and chemistry of formaldehyde by mesoscale convective systems in West Africa during AMMA 2006, *Journal of Geophysical Research: Atmospheres*, 117, , 2012.
- 680



- Brocchi, V., Krysztofiak, G., Catoire, V., Guth, J., Marecal, V., Zbinden, R., Amraoui, L. E., Dulac, F., and Ricaud, P.: Intercontinental transport of biomass burning pollutants over the Mediterranean Basin during the summer 2014 ChArMEx-GLAM airborne campaign, *Atmospheric Chemistry and Physics*, 18, 6887–6906, 2018.
- Burrows, J., Dehn, A., Deters, B., Himmelmann, S., Richter, A., Voigt, S., and Orphal, J.: Atmospheric remote-sensing reference data from GOME: Part 1. Temperature-dependent absorption cross-sections of NO₂ in the 231–794 nm range, *Journal of Quantitative Spectroscopy and Radiative Transfer*, 60, 1025–1031, 1998.
- 685 Carlier, P., Hannachi, H., and Mouvier, G.: The chemistry of carbonyl compounds in the atmosphere—A review, *Atmospheric Environment* (1967), 20, 2079 – 2099, [https://doi.org/https://doi.org/10.1016/0004-6981\(86\)90304-5](https://doi.org/https://doi.org/10.1016/0004-6981(86)90304-5), <http://www.sciencedirect.com/science/article/pii/0004698186903045>, 1986.
- 690 Chan Miller, C., Gonzalez Abad, G., Wang, H., Liu, X., Kurosu, T., Jacob, D. J., and Chance, K.: Glyoxal retrieval from the Ozone Monitoring Instrument, *Atmospheric Measurement Techniques*, 7, 3891–3907, <https://doi.org/10.5194/amt-7-3891-2014>, <https://www.atmos-meas-tech.net/7/3891/2014/>, 2014.
- Chan Miller, C., Jacob, D. J., Marais, E. A., Yu, K., Travis, K. R., Kim, P. S., Fisher, J. A., Zhu, L., Wolfe, G. M., Hanisco, T. F., Keutsch, F. N., Kaiser, J., Min, K.-E., Brown, S. S., Washenfelder, R. A., González Abad, G., and Chance, K.: Glyoxal yield from isoprene oxidation and relation to formaldehyde: chemical mechanism, constraints from SENEX aircraft observations, and interpretation of OMI satellite data, *Atmospheric Chemistry and Physics*, 17, 8725–8738, <https://doi.org/10.5194/acp-17-8725-2017>, <https://www.atmos-chem-phys.net/17/8725/2017/>, 2017.
- 695 Chance, K. and Orphal, J.: Revised ultraviolet absorption cross sections of H₂CO for the HITRAN database, *Journal of Quantitative Spectroscopy and Radiative Transfer*, 112, 1509–1510, 2011.
- 700 Crutzen, P. J. and Andreae, M. O.: Biomass Burning in the Tropics: Impact on Atmospheric Chemistry and Biogeochemical Cycles, *Science*, 250, 1669–1678, <https://doi.org/10.1126/science.250.4988.1669>, <http://science.sciencemag.org/content/250/4988/1669>, 1990.
- De Smedt, I., Müller, J.-F., Stavrou, T., van der A, R., Eskes, H., and Van Roozendael, M.: Twelve years of global observations of formaldehyde in the troposphere using GOME and SCIAMACHY sensors, *Atmospheric Chemistry and Physics*, 8, 4947–4963, <https://doi.org/10.5194/acp-8-4947-2008>, <https://www.atmos-chem-phys.net/8/4947/2008/>, 2008a.
- 705 De Smedt, I., Müller, J.-F., Stavrou, T., Van Der A, R., Eskes, H., and Van Roozendael, M.: Twelve years of global observations of formaldehyde in the troposphere using GOME and SCIAMACHY sensors, *Atmos. Chem. Phys.*, 2008b.
- De Smedt, I., Stavrou, T., Hendrick, F., Danckaert, T., Vlemmix, T., Pinardi, G., Theys, N., Lerot, C., Gielen, C., Vigouroux, C., et al.: Diurnal, seasonal and long-term variations of global formaldehyde columns inferred from combined OMI and GOME-2 observations., *Atmospheric Chemistry & Physics Discussions*, 15, 2015.
- 710 Deutschmann, T., Beirle, S., Frieß, U., Grzegorski, M., Kern, C., Kritten, L., Platt, U., Pukite, J., Wagner, T., Werner, B., and Pfeilsticker, K.: The Monte Carlo Atmospheric Radiative Transfer Model McArtim: Introduction and Validation of Jacobians and 3D Features, *Journal of Quantitative Spectroscopy and Radiative Transfer*, 112, 1119–1137, 2011.
- DiGangi, J., Henry, S., Kammrath, A., Boyle, E., Kaser, L., Schnitzhofer, R., Graus, M., Turnipseed, A., Park, J., Weber, R., et al.: Observations of glyoxal and formaldehyde as metrics for the anthropogenic impact on rural photochemistry, *Atmospheric Chemistry and Physics*, 12, 9529–9543, 2012.
- 715 Dufour, G., Szopa, S., Barkley, M. P., Boone, C. D., Perrin, A., Palmer, P. I., and Bernath, P. F.: Global upper-tropospheric formaldehyde: seasonal cycles observed by the ACE-FTS satellite instrument, *Atmospheric Chemistry and Physics*, 9, 3893–3910, <https://doi.org/10.5194/acp-9-3893-2009>, <https://www.atmos-chem-phys.net/9/3893/2009/>, 2009.



- 720 Finlayson-Pitts, B. J. and Pitts, J. N.: Photochemistry of Important Atmospheric Species, Academic Press, San Diego, <https://doi.org/https://doi.org/10.1016/B978-012257060-5/50006-X>, <http://www.sciencedirect.com/science/article/pii/B978012257060550006X>, 2000.
- 725 Fried, A., Olson, J. R., Walega, J. G., Crawford, J. H., Chen, G., Weibring, P., Richter, D., Roller, C., Tittel, F., Porter, M., Fuelberg, H., Halland, J., Bertram, T. H., Cohen, R. C., Pickering, K., Heikes, B. G., Snow, J. A., Shen, H., O'Sullivan, D. W., Brune, W. H., Ren, X., Blake, D. R., Blake, N., Sachse, G., Diskin, G. S., Podolske, J., Vay, S. A., Shetter, R. E., Hall, S. R., Anderson, B. E., Thornhill, L., Clarke, A. D., McNaughton, C. S., Singh, H. B., Avery, M. A., Huey, G., Kim, S., and Millet, D. B.: Role of convection in redistributing formaldehyde to the upper troposphere over North America and the North Atlantic during the summer 2004 INTEX campaign, *Journal of Geophysical Research: Atmospheres*, 113, <https://doi.org/10.1029/2007JD009760>, <https://agupubs.onlinelibrary.wiley.com/doi/abs/10.1029/2007JD009760>, 2008.
- 730 Frost, G., Fried, A., Lee, Y.-N., Wert, B., Henry, B., Drummond, J., Evans, M., Fehsenfeld, F. C., Goldan, P., Holloway, J., et al.: Comparisons of box model calculations and measurements of formaldehyde from the 1997 North Atlantic Regional Experiment, *Journal of Geophysical Research: Atmospheres*, 107, ACH-3, 2002.
- Fu, D., Millet, D. B., Wells, K. C., Payne, V. H., Yu, S., Guenther, A., and Eldering, A.: Direct retrieval of isoprene from satellite-based infrared measurements, *Nature communications*, 10, 1–12, 2019.
- 735 Fu, T.-M., Jacob, D. J., Wittrock, F., Burrows, J. P., Vrekoussis, M., and Henze, D. K.: Global budgets of atmospheric glyoxal and methylglyoxal, and implications for formation of secondary organic aerosols, *Journal of Geophysical Research: Atmospheres*, 113, , <https://doi.org/10.1029/2007JD009505>, <https://agupubs.onlinelibrary.wiley.com/doi/abs/10.1029/2007JD009505>, 2008.
- Gerbig, C., Kley, D., Volz-Thomas, A., Kent, J., Dewey, K., and McKenna, D. S.: Fast response resonance fluorescence CO measurements aboard the C-130: Instrument characterization and measurements made during North Atlantic Regional Experiment 1993, *Journal of Geophysical Research: Atmospheres*, 101, 29 229–29 238, 1996.
- 740 Gerbig, C., Schmitgen, S., Kley, D., Volz-Thomas, A., Dewey, K., and Haaks, D.: An improved fast-response vacuum-UV resonance fluorescence CO instrument, *Journal of Geophysical Research: Atmospheres*, 104, 1699–1704, 1999.
- Gu, D., Guenther, A. B., Shilling, J. E., Yu, H., Huang, M., Zhao, C., Yang, Q., Martin, S. T., Artaxo, P., Kim, S., et al.: Airborne observations reveal elevational gradient in tropical forest isoprene emissions, *Nature communications*, 8, 1–7, 2017.
- 745 Hays, M. D., Geron, C. D., Linna, K. J., Smith, N. D., and Schauer, J. J.: Speciation of Gas-Phase and Fine Particle Emissions from Burning of Foliar Fuels, *Environmental Science & Technology*, 36, 2281–2295, <https://doi.org/10.1021/es0111683>, <https://doi.org/10.1021/es0111683>, PMID: 12075778, 2002.
- Helmig, D., Balsley, B., Davis, K., Kuck, L. R., Jensen, M., Bogner, J., Smith Jr, T., Arrieta, R. V., Rodríguez, R., and Birks, J. W.: Vertical profiling and determination of landscape fluxes of biogenic nonmethane hydrocarbons within the planetary boundary layer in the Peruvian Amazon, *Journal of Geophysical Research: Atmospheres*, 103, 25 519–25 532, 1998.
- 750 Horowitz, A., Meller, R., and Moortgat, G. K.: The UV–VIS absorption cross sections of the α -dicarbonyl compounds: pyruvic acid, biacetyl and glyoxal, *Journal of Photochemistry and Photobiology A: Chemistry*, 146, 19–27, 2001.
- Hüneke, T.: The scaling method applied to HALO measurements: Inferring absolute trace gas concentrations from airborne limb spectroscopy under all sky conditions, Phd, University of Heidelberg, Heidelberg, Germany, <http://www.iup.uni-heidelberg.de/institut/forschung/groups/atmosphere/stratosphere/Theses/>, 2016.
- 755 Hüneke, T., Aderhold, O.-A., Bounin, J., Dorf, M., Gentry, E., Grossmann, K., Groß, J.-U., Hoor, P., Jöckel, P., Kenntner, M., Knapp, M., Knecht, M., Lörks, D., Ludmann, S., Matthes, S., Raecke, R., Reichert, M., Weimar, J., Werner, B., Zahn, A., Ziereis, H., and



- Pfeilsticker, K.: The novel HALO mini-DOAS instrument: inferring trace gas concentrations from airborne UV/visible limb spectroscopy under all skies using the scaling method, *Atmospheric Measurement Techniques*, 10, 4209–4234, <https://doi.org/10.5194/amt-10-4209-2017>, <https://www.atmos-meas-tech.net/10/4209/2017/>, 2017.
- 760 Huntrieser, H., Lichtenstern, M., Scheibe, M., Aufmhoff, H., Schlager, H., Pucik, T., Minikin, A., Weinzierl, B., Heimerl, K., Fütterer, D., et al.: On the origin of pronounced O₃ gradients in the thunderstorm outflow region during DC3, *Journal of Geophysical Research: Atmospheres*, 121, 6600–6637, 2016a.
- Huntrieser, H., Lichtenstern, M., Scheibe, M., Aufmhoff, H., Schlager, H., Pucik, T., Minikin, A., Weinzierl, B., Heimerl, K., Pollack, I., et al.: Injection of lightning-produced NO_x, water vapor, wildfire emissions, and stratospheric air to the UT/LS as observed from DC3
765 measurements, *Journal of Geophysical Research: Atmospheres*, 121, 6638–6668, 2016b.
- Jaeglé, L., Jacob, D. J., Wennberg, P. O., Spivakovsky, C. M., Hanisco, T. F., Lanzendorf, E. J., Hints, E. J., Fahey, D. W., Keim, E. R., Proffitt, M. H., Atlas, E. L., Flocke, F., Schauffler, S., McElroy, C. T., Midwinter, C., Pfister, L., and Wilson, J. C.: Observed OH and HO₂ in the upper troposphere suggest a major source from convective injection of peroxides, *Geophysical Research Letters*, 24, 3181–3184, <https://doi.org/10.1029/97GL03004>, <https://agupubs.onlinelibrary.wiley.com/doi/abs/10.1029/97GL03004>, 1997.
- 770 Kaiser, J., Wolfe, G. M., Min, K. E., Brown, S. S., Miller, C. C., Jacob, D. J., deGouw, J. A., Graus, M., Hanisco, T. F., Holloway, J., Peischl, J., Pollack, I. B., Ryerson, T. B., Warneke, C., Washenfelder, R. A., and Keutsch, F. N.: Reassessing the ratio of glyoxal to formaldehyde as an indicator of hydrocarbon precursor speciation, *Atmospheric Chemistry and Physics*, 15, 7571–7583, <https://doi.org/10.5194/acp-15-7571-2015>, <https://www.atmos-chem-phys.net/15/7571/2015/>, 2015.
- Kesselmeier, J., Kuhn, U., Wolf, A., Andreae, M., Ciccioli, P., Brancaleoni, E., Frattoni, M., Guenther, A., Greenberg, J., Vasconcellos, P.
775 D. C., et al.: Atmospheric volatile organic compounds (VOC) at a remote tropical forest site in central Amazonia, *Atmospheric Environment*, 34, 4063–4072, 2000.
- Knecht, M.: Simulation of radiative field modification due to tropical clouds, Master thesis, Institut für Umweltphysik, Universität Heidelberg, http://www.iup.uni-heidelberg.de/institut/forschung/groups/atmosphere/stratosphere/publications/pdf/MA_thesis_Matthias_final.pdf, 2015.
- 780 Knote, C., Hodzic, A., Jimenez, J. L., Volkamer, R., Orlando, J. J., Baidar, S., Brioude, J., Fast, J., Gentner, D. R., Goldstein, A. H., Hayes, P. L., Knighton, W. B., Oetjen, H., Setyan, A., Stark, H., Thalman, R., Tyndall, G., Washenfelder, R., Waxman, E., and Zhang, Q.: Simulation of semi-explicit mechanisms of SOA formation from glyoxal in aerosol in a 3-D model, *Atmospheric Chemistry and Physics*, 14, 6213–6239, <https://doi.org/10.5194/acp-14-6213-2014>, <https://www.atmos-chem-phys.net/14/6213/2014/>, 2014.
- Koch, S. and Moortgat, G. K.: Photochemistry of methylglyoxal in the vapor phase, *The Journal of Physical Chemistry A*, 102, 9142–9153,
785 1998.
- Krysztofiak, G., Catoire, V., Hamer, P. D., Marecal, V., Robert, C., Engel, A., Bönisch, H., Grossmann, K., Quack, B., Atlas, E., et al.: Evidence of convective transport in tropical West Pacific region during SHIVA experiment, *Atmospheric Science Letters*, 19, e798, 2018.
- Kuhn, U., Andreae, M., Ammann, C., Araújo, A., Brancaleoni, E., Ciccioli, P., Dindorf, T., Frattoni, M., Gatti, L., Ganzeveld, L., et al.: Isoprene and monoterpene fluxes from Central Amazonian rainforest inferred from tower-based and airborne measurements, and implications
790 on the atmospheric chemistry and the local carbon budget, *Atmospheric Chemistry and Physics*, 7, 2855–2879, 2007.
- Lawson, S. J., Selleck, P. W., Galbally, I. E., Keywood, M. D., Harvey, M. J., Lerot, C., Helmig, D., and Ristovski, Z.: Seasonal in situ observations of glyoxal and methylglyoxal over the temperate oceans of the Southern Hemisphere, *Atmospheric Chemistry and Physics*, 15, 223–240, <https://doi.org/10.5194/acp-15-223-2015>, <https://www.atmos-chem-phys.net/15/223/2015/>, 2015.



- 795 Lerot, C., Stavrou, T., De Smedt, I., Müller, J.-F., and Van Roozendael, M.: Glyoxal vertical columns from GOME-2 backscattered light measurements and comparisons with a global model, *Atmospheric Chemistry and Physics*, 10, 12 059–12 072, <https://doi.org/10.5194/acp-10-12059-2010>, <https://www.atmos-chem-phys.net/10/12059/2010/>, 2010.
- 800 Li, J., Mao, J., Min, K.-E., Washenfelder, R. A., Brown, S. S., Kaiser, J., Keutsch, F. N., Volkamer, R., Wolfe, G. M., Hanisco, T. F., Pollack, I. B., Ryerson, T. B., Graus, M., Gilman, J. B., Lerner, B. M., Warneke, C., Gouw, J. A., Middlebrook, A. M., Liao, J., Welti, A., Henderson, B. H., McNeill, V. F., Hall, S. R., Ullmann, K., Donner, L. J., Paulot, F., and Horowitz, L. W.: Observational constraints on glyoxal production from isoprene oxidation and its contribution to organic aerosol over the Southeast United States, *Journal of Geophysical Research: Atmospheres*, 121, 9849–9861, <https://doi.org/10.1002/2016JD025331>, <https://agupubs.onlinelibrary.wiley.com/doi/abs/10.1002/2016JD025331>, 2016.
- 805 Liao, J., Hanisco, T. F., Wolfe, G. M., St. Clair, J., Jimenez, J. L., Campuzano-Jost, P., Nault, B. A., Fried, A., Marais, E. A., Gonzalez Abad, G., Chance, K., Jethva, H. T., Ryerson, T. B., Warneke, C., and Wisthaler, A.: Towards a satellite formaldehyde – in situ hybrid estimate for organic aerosol abundance, *Atmospheric Chemistry and Physics*, 19, 2765–2785, <https://doi.org/10.5194/acp-19-2765-2019>, <https://www.atmos-chem-phys.net/19/2765/2019/>, 2019.
- Lim, C. Y., Hagan, D. H., Coggon, M. M., Koss, A. R., Sekimoto, K., de Gouw, J., Warneke, C., Cappa, C. D., and Kroll, J. H.: Secondary organic aerosol formation from biomass burning emissions, *Atmospheric Chemistry and Physics Discussions*, 2019, 1–23, <https://doi.org/10.5194/acp-2019-326>, <https://www.atmos-chem-phys-discuss.net/acp-2019-326/>, 2019.
- 810 MacDonald, S., Oetjen, H., Mahajan, A., Whalley, L., Edwards, P., Heard, D., Jones, C., and Plane, J.: DOAS measurements of formaldehyde and glyoxal above a south-east Asian tropical rainforest, *Atmospheric Chemistry and Physics*, 12, 5949–5962, 2012.
- McDonald, J. D., Zielinska, B., Fujita, E. M., Sagebiel, J. C., Chow, J. C., and Watson, J. G.: Fine Particle and Gaseous Emission Rates from Residential Wood Combustion, *Environmental Science & Technology*, 34, 2080–2091, <https://doi.org/10.1021/es9909632>, <https://doi.org/10.1021/es9909632>, 2000a.
- 815 McDonald, J. D., Zielinska, B., Fujita, E. M., Sagebiel, J. C., Chow, J. C., and Watson, J. G.: Fine particle and gaseous emission rates from residential wood combustion, *Environmental Science & Technology*, 34, 2080–2091, 2000b.
- Meller, R., Raber, W., Crowley, J., Jenkin, M., and Moortgat, G.: The UV-visible absorption spectrum of methylglyoxal, *Journal of Photochemistry and Photobiology A: Chemistry*, 62, 163–171, 1991.
- 820 Michoud, V., Sauvage, S., Léonardis, T., Fronval, I., Kukui, A., Locoge, N., and Dusanter, S.: Field measurements of methylglyoxal using proton transfer reaction time-of-flight mass spectrometry and comparison to the DNPH–HPLC–UV method, *Atmospheric Measurement Techniques*, 11, 5729–5740, <https://doi.org/10.5194/amt-11-5729-2018>, <https://www.atmos-meas-tech.net/11/5729/2018/>, 2018.
- Müller, M., Anderson, B. E., Beyersdorf, A. J., Crawford, J. H., Diskin, G. S., Eichler, P., Fried, A., Keutsch, F. N., Mikoviny, T., Thornhill, K. L., et al.: In situ measurements and modeling of reactive trace gases in a small biomass burning plume, *Atmospheric Chemistry and Physics*, 16, 3813–3824, 2016.
- 825 Myriokefalitakis, S., Vrekoussis, M., Tsigaridis, K., Wittrock, F., Richter, A., Brühl, C., Volkamer, R., Burrows, J. P., and Kanakidou, M.: The influence of natural and anthropogenic secondary sources on the glyoxal global distribution, *Atmospheric Chemistry and Physics*, 8, 4965–4981, <https://doi.org/10.5194/acp-8-4965-2008>, <https://www.atmos-chem-phys.net/8/4965/2008/>, 2008.
- Pang, X., Lewis, A., and Hamilton, J.: Determination of airborne carbonyls via pentafluorophenylhydrazine derivatisation by GC-MS and its comparison with HPLC method, *Talanta*, 85, 406–414, <https://doi.org/10.1016/j.talanta.2011.03.072>, 2011.



- 830 Peters, E., Wittrock, F., Großmann, K., Frieß, U., Richter, A., and Burrows, J. P.: Formaldehyde and nitrogen dioxide over the remote western Pacific Ocean: SCIAMACHY and GOME-2 validation using ship-based MAX-DOAS observations, *Atmospheric Chemistry and Physics*, 12, 11 179–11 197, <https://doi.org/10.5194/acp-12-11179-2012>, <https://www.atmos-chem-phys.net/12/11179/2012/>, 2012.
- Platt, U. and Stutz, J.: *Differential Optical Absorption Spectroscopy (DOAS), Principle and Applications*, no. ISBN 978-3-642-05946-9 in ISSN 1610-1677, Springer Verlag, Heidelberg, <https://doi.org/10.1007/978-3-540-75776-40>, 2008.
- 835 Pöschl, U., Williams, J., Hoor, P., Fischer, H., Crutzen, P., Warneke, C., Holzinger, R., Hansel, A., Jordan, A., Lindinger, W., et al.: High acetone concentrations throughout the 0–12 km altitude range over the tropical rainforest in Surinam, *Journal of atmospheric chemistry*, 38, 115–132, 2001.
- Rizzo, L., Artaxo, P., Karl, T., Guenther, A., and Greenberg, J.: Aerosol properties, in-canopy gradients, turbulent fluxes and VOC concentrations at a pristine forest site in Amazonia, *Atmospheric Environment*, 44, 503–511, 2010.
- 840 Rolph, G., Stein, A., and Stunder, B.: Real-time environmental applications and display system: READY, *Environmental Modelling & Software*, 95, 210–228, 2017.
- Rothman, L. S., Gordon, I. E., Barbe, A., Benner, D. C., Bernath, P. F., Birk, M., Boudon, V., Brown, L. R., Campargue, A., and Champion et al., J.-P.: The HITRAN 2008 molecular spectroscopic database, *Journal of Quantitative Spectroscopy and Radiative Transfer*, 110, 533–572, 2009.
- 845 Sander, R.: Compilation of Henry’s law constants (version 4.0) for water as solvent, *Atmos. Chem. Phys.*, 15, 4399–4981, 2015.
- Schulz, C., Schneider, J., Amorim Holanda, B., Appel, O., Costa, A., Sá, S. S. d., Dreiling, V., Fütterer, D., Jurkat-Witschas, T., Klimach, T., et al.: Aircraft-based observations of isoprene-epoxydiol-derived secondary organic aerosol (IEPOX-SOA) in the tropical upper troposphere over the Amazon region, *Atmospheric Chemistry and Physics*, 18, 14 979–15 001, 2018.
- Seinfeld, J. H. and Pandis, S. N.: *Atmospheric chemistry and physics : from air pollution to climate change*, ISBN 9780471720171, J. Wiley & Sons, Inc., third edition edn., 2013.
- 850 Serdyuchenko, A., Gorshchev, V., Weber, M., Chehade, W., and Burrows, J. P.: High spectral resolution ozone absorption cross-sections - Part 2: Temperature dependence, *Atmospheric Measurement Techniques*, 7, 625–636, <https://doi.org/10.5194/amt-7-625-2014>, <http://www.atmos-meas-tech.net/7/625/2014/>, 2014.
- Stavroukou, T., Müller, J.-F., De Smedt, I., Van Roozendael, M., van der Werf, G. R., Giglio, L., and Guenther, A.: Evaluating the performance of pyrogenic and biogenic emission inventories against one decade of space-based formaldehyde columns, *Atmospheric Chemistry and Physics*, 9, 1037–1060, <https://doi.org/10.5194/acp-9-1037-2009>, <https://www.atmos-chem-phys.net/9/1037/2009/>, 2009.
- 855 Stavroukou, T., Müller, J.-F., Bauwens, M., De Smedt, I., Lerot, C., Van Roozendael, M., Coheur, P.-F., Clerbaux, C., Boersma, K. F., van der A, R., and Song, Y.: Substantial Underestimation of Post-Harvest Burning Emissions in the North China Plain Revealed by Multi-Species Space Observations, *Scientific Reports*, 6, <https://doi.org/10.1038/srep32307>, <https://doi.org/10.1038/srep32307>, 2016.
- 860 Steck, T., Glatthor, N., von Clarmann, T., Fischer, H., Flaud, J. M., Funke, B., Grabowski, U., Höpfner, M., Kellmann, S., Linden, A., Perrin, A., and Stiller, G. P.: Retrieval of global upper tropospheric and stratospheric formaldehyde (H₂CO) distributions from high-resolution MIPAS-Envisat spectra, *Atmospheric Chemistry and Physics*, 8, 463–470, <https://doi.org/10.5194/acp-8-463-2008>, <https://www.atmos-chem-phys.net/8/463/2008/>, 2008.
- Stein, A., Draxler, R. R., Rolph, G. D., Stunder, B. J., Cohen, M., and Ngan, F.: NOAA’s HYSPLIT atmospheric transport and dispersion modeling system, *Bulletin of the American Meteorological Society*, 96, 2059–2077, 2015.
- 865



- Stockwell, C. E., Veres, P. R., Williams, J., and Yokelson, R. J.: Characterization of biomass burning emissions from cooking fires, peat, crop residue, and other fuels with high-resolution proton-transfer-reaction time-of-flight mass spectrometry, *Atmospheric Chemistry and Physics*, 15, 845–865, <https://doi.org/10.5194/acp-15-845-2015>, <https://www.atmos-chem-phys.net/15/845/2015/>, 2015.
- 870 Stutz, J., Werner, B., Spolaor, M., Scalone, L., Festa, J., Tsai, C., Cheung, R., Colosimo, S. F., Tricoli, U., Raecke, R., Hossaini, R., Chipperfield, M. P., Feng, W., Gao, R.-S., Hintsä, E. J., Elkins, J. W., Moore, F. L., Daube, B., Pittman, J., Wofsy, S., and Pfeilsticker, K.: A new Differential Optical Absorption Spectroscopy instrument to study atmospheric chemistry from a high-altitude unmanned aircraft, *Atmospheric Measurement Techniques*, 10, 1017 – 1042, <https://doi.org/10.5194/amt-10-1017-2017>, <http://www.atmos-meas-tech.net/10/1017/2017/>, 2017.
- 875 Tadić, J., Moortgat, G. K., and Wirtz, K.: Photolysis of glyoxal in air, *Journal of Photochemistry and Photobiology A: Chemistry*, 177, 116–124, 2006.
- Thalman, R. and Volkamer, R.: Inherent calibration of a blue LED-CE-DOAS instrument to measure iodine oxide, glyoxal, methyl glyoxal, nitrogen dioxide, water vapour and aerosol extinction in open cavity mode, *Atmospheric Measurement Techniques*, 3, 1797–1814, <https://doi.org/10.5194/amt-3-1797-2010>, <https://www.atmos-meas-tech.net/3/1797/2010/>, 2010.
- 880 Thalman, R. and Volkamer, R.: Temperature dependent absorption cross-sections of O₂-O₂ collision pairs between 340 and 630 nm and at atmospherically relevant pressure, *Phys. Chem. Chem. Phys.*, 15, 15 371–15 381, <https://doi.org/10.1039/C3CP50968K>, <http://dx.doi.org/10.1039/C3CP50968K>, 2013.
- 885 Thalman, R., Baeza-Romero, M. T., Ball, S. M., Borrás, E., Daniels, M. J. S., Goodall, I. C. A., Henry, S. B., Karl, T., Keutsch, F. N., Kim, S., Mak, J., Monks, P. S., Muñoz, A., Orlando, J., Peppe, S., Rickard, A. R., Ródenas, M., Sánchez, P., Seco, R., Su, L., Tyndall, G., Vázquez, M., Vera, T., Waxman, E., and Volkamer, R.: Instrument intercomparison of glyoxal, methyl glyoxal and NO₂ under simulated atmospheric conditions, *Atmospheric Measurement Techniques*, 8, 1835–1862, <https://doi.org/10.5194/amt-8-1835-2015>, <https://www.atmos-meas-tech.net/8/1835/2015/>, 2015.
- Volkamer, R., Molina, L. T., Molina, M. J., Shirley, T., and Brune, W. H.: DOAS measurement of glyoxal as an indicator for fast VOC chemistry in urban air, *Geophysical Research Letters*, 32, <https://doi.org/10.1029/2005GL022616>, <https://agupubs.onlinelibrary.wiley.com/doi/abs/10.1029/2005GL022616>, 2005a.
- 890 Volkamer, R., Spietz, P., Burrows, J., and Platt, U.: High-resolution absorption cross-section of glyoxal in the UV–vis and IR spectral ranges, *Journal of Photochemistry and Photobiology A: Chemistry*, 172, 35–46, 2005b.
- Vrekoussis, M., Wittrock, F., Richter, A., and Burrows, J.: Temporal and spatial variability of glyoxal as observed from space, *Atmospheric Chemistry and Physics*, 9, 4485–4504, 2009.
- 895 Vrekoussis, M., Wittrock, F., Richter, A., and Burrows, J. P.: GOME-2 observations of oxygenated VOCs: what can we learn from the ratio glyoxal to formaldehyde on a global scale?, *Atmospheric Chemistry and Physics*, 10, 10 145–10 160, <https://doi.org/10.5194/acp-10-10145-2010>, <https://www.atmos-chem-phys.net/10/10145/2010/>, 2010.
- Wagner, V., von Glasow, R., Fischer, H., and Crutzen, P. J.: Are CH₂O measurements in the marine boundary layer suitable for testing the current understanding of CH₄ photooxidation?: A model study, *Journal of Geophysical Research: Atmospheres*, 107, ACH 3–1–ACH 3–14, <https://doi.org/10.1029/2001JD000722>, <https://agupubs.onlinelibrary.wiley.com/doi/abs/10.1029/2001JD000722>, 2002.
- 900 Wang, M., Shao, M., Chen, W., Yuan, B., Lu, S., Zhang, Q., Zeng, L., and Wang, Q.: Atmospheric nanoparticles formed from heterogeneous reactions of organics, *Nature Geoscience*, 3, 238–24, <https://doi.org/10.1038/ngeo778>, <https://www.nature.com/articles/ngeo778>, 2010.



- Warneke, C., Karl, T., Judmaier, H., Hansel, A., Jordan, A., Lindinger, W., and Crutzen, P. J.: Acetone, methanol, and other partially oxidized volatile organic emissions from dead plant matter by abiological processes: Significance for atmospheric HO_x chemistry, *Global Biogeochemical Cycles*, 13, 9–17, 1999.
- 905 Warneke, C., Holzinger, R., Hansel, A., Jordan, A., Lindinger, W., Pöschl, U., Williams, J., Hoor, P., Fischer, H., Crutzen, P., et al.: Isoprene and its oxidation products methyl vinyl ketone, methacrolein, and isoprene related peroxides measured online over the tropical rain forest of Surinam in March 1998, *Journal of Atmospheric Chemistry*, 38, 167–185, 2001.
- Wendisch, M., Pöschl, U., Andreae, M. O., Machado, L. A. T., Albrecht, R., Schlager, H., Rosenfeld, D., Martin, S. T., Abdelmonem, A., Afchine, A., Araújo, A. C., Artaxo, P., Aufmhoff, H., Barbosa, H. M. J., Borrmann, S., Braga, R., Buchholz, B., Cecchini, M. A., Costa, A., Curtius, J., Dollner, M., Dorf, M., Dreiling, V., Ebert, V., Ehrlich, A., Ewald, F., Fisch, G., Fix, A., Frank, F., Fütterer, D., Heckl, C., Heidelberg, F., Hüeneke, T., Jäkel, E., Järvinen, E., Jurkat, T., Kanter, S., Kästner, U., Kenntner, M., Kesselmeier, J., Klimach, T., Knecht, M., Kohl, R., Kölling, T., Krämer, M., Krüger, M., Krisna, T. C., Lavric, J. V., Longo, K., Mahnke, C., Manzi, A. O., Mayer, B., Mertes, S., Minikin, A., Molleker, S., Münch, S., Nillius, B., Pfeilsticker, K., Pöhlker, C., Roiger, A., Rose, D., Rosenow, D., Sauer, D., Schnaiter, M., Schneider, J., Schulz, C., de Souza, R. A. F., Spanu, A., Stock, P., Vila, D., Voigt, C., Walser, A., Walter, D., Weigel, R., Weinzierl, B., Werner, F., Yamasoe, M. A., Ziereis, H., Zinner, T., and Zöger, M.: ACRIDICON–CHUVA Campaign: Studying Tropical Deep Convective Clouds and Precipitation over Amazonia Using the New German Research Aircraft HALO, *Bulletin of the American Meteorological Society*, 97, 1885–1908, <https://doi.org/10.1175/BAMS-D-14-00255.1>, <https://doi.org/10.1175/BAMS-D-14-00255.1>, 2016.
- 915 Wennberg, P. O., Bates, K. H., Crouse, J. D., Dodson, L. G., McVay, R. C., Mertens, L. A., Nguyen, T. B., Praske, E., Schwantes, R. H., Smarte, M. D., St Clair, J. M., Teng, A. P., Zhang, X., and Seinfeld, J. H.: Gas-Phase Reactions of Isoprene and Its Major Oxidation Products, *Chemical Reviews*, 118, 3337–3390, <https://doi.org/10.1021/acs.chemrev.7b00439>, <https://doi.org/10.1021/acs.chemrev.7b00439>, PMID: 29522327, 2018.
- 920 Werner, B., Stutz, J., Spolaor, M., Scalone, L., Raecke, R., Festa, J., Colosimo, S. F., Cheung, R., Tsai, C., Hossaini, R., Chipperfield, M. P., Taverna, G. S., Feng, W., Elkins, J. W., Fahey, D. W., Gao, R.-S., Hints, E. J., Thornberry, T. D., Moore, F. L., Navarro, M. A., Atlas, E., Daube, B. C., Pittman, J., Wofsy, S., and Pfeilsticker, K.: Probing the subtropical lowermost stratosphere and the tropical upper troposphere and tropopause layer for inorganic bromine, *Atmospheric Chemistry and Physics*, 17, 1161–1186, <https://doi.org/10.5194/acp-17-1161-2017>, <http://www.atmos-chem-phys.net/17/1161/2017/>, 2017.
- Williamson, C. J., Kupc, A., Axisa, D., Bilsback, K. R., Bui, T., Campuzano-Jost, P., Dollner, M., Froyd, K. D., Hodshire, A. L., Jimenez, J. L., et al.: A large source of cloud condensation nuclei from new particle formation in the tropics, *Nature*, 574, 399–403, 2019.
- 930 Wittrock, F., Richter, A., Oetjen, H., Burrows, J. P., Kanakidou, M., Myriokefalitakis, S., Volkamer, R., Beirle, S., Platt, U., and Wagner, T.: Simultaneous global observations of glyoxal and formaldehyde from space, *Geophysical Research Letters*, 33, , <https://doi.org/10.1029/2006GL026310>, <https://agupubs.onlinelibrary.wiley.com/doi/abs/10.1029/2006GL026310>, 2006.
- Zarzana, K. J., Min, K.-E., Washenfelder, R. A., Kaiser, J., Krawiec-Thayer, M., Peischl, J., Neuman, J. A., Nowak, J. B., Wagner, N. L., Dubè, W. P., St. Clair, J. M., Wolfe, G. M., Hanisco, T. F., Keutsch, F. N., Ryerson, T. B., and Brown, S. S.: Emissions of Glyoxal and Other Carbonyl Compounds from Agricultural Biomass Burning Plumes Sampled by Aircraft, *Environmental Science & Technology*, 51, 11 761–11 770, <https://doi.org/10.1021/acs.est.7b03517>, <https://doi.org/10.1021/acs.est.7b03517>, PMID: 28976736, 2017.
- 935 Zarzana, K. J., Selimovic, V., Koss, A. R., Sekimoto, K., Coggon, M. M., Yuan, B., Dubé, W. P., Yokelson, R. J., Warneke, C., de Gouw, J. A., Roberts, J. M., and Brown, S. S.: Primary emissions of glyoxal and methylglyoxal from laboratory measurements of open biomass burning, *Atmospheric Chemistry and Physics*, 18, 15 451–15 470, <https://doi.org/10.5194/acp-18-15451-2018>, <https://www.atmos-chem-phys.net/18/15451/2018/>, 2018.